



Université Grenoble Alpes

Report

Mid-term

MIRA Anna

Supervisors:

Yohan Payan, TIMC-IMAG Lab, CNRS & Univ. Grenoble Alpes
Serge Muller, GE-Healthcare, France
Ann-Katherine Carton, GE-Healthcare, France

V1

Grenoble, September 2016

Contents

Contents  iii

List of Figures  vii

5 List of Tables  ix

1	Introduction	1
1.1	General Problem statement	1
1.2	Technical approach	1
1.3	Thesis overview	1
10	1.4 Key contributions	1
1.5	Software	1
1.6	Ethics	1

I Background  3

2	Clinical background	4
15	2.1 Introduction	4
	2.2 Breast anatomy	4
	2.2.1 Breast embryogenesis	4
	2.2.2 Breast Appearance	5
	2.2.3 Internal structure	6
20	2.2.4 Adult breast texture changes	9
	2.3 Breast Cancer	10
	2.3.1 Cancer classification	11
	2.3.2 Breast cancer screening	12
25	2.4 Medical Imaging	12
	2.4.1 X-ray mammography	12
	2.4.2 Ultrasounds	14
	2.4.3 Magnetic resonance imaging	14
	2.5 Conclusion	15

Report iii

CONTENTS

II	Biomechanical breast modeling		17	
30	3	Background and state of the art	18	
30	3.1	Introduction	18	
30	3.2	Continuous mechanics	18	
35	3.2.1	Deformation and strain	18	
35	3.2.2	Stress measures	22	
35	3.2.3	Conservation equations	24	
35	3.2.4	Constitutive models	25	
40	3.3	Finite Element Discretization	28	
40	3.3.1	Eulerian and Lagrangian mesh description	28	
40	3.3.2	Lagrangian mesh	29	
40	3.4	Contact mechanics	32	
40	3.4.1	Contact interface equations	33	
40	3.4.2	Surface interaction models	34	
40	3.4.3	Contact formulation algorithm: Pure Penalty model	35	
45	3.5	Breast biomechanical model: overview	37	
45	3.5.1	Breast reference configuration	38	
45	3.5.2	Constitutive models	40	
45	3.5.3	Boundary conditions	43	
45	3.5.4	Conclusion	43	
50	4	A new biomechanical breast model	46	
50	4.1	Introduction	46	
50	4.2	Data acquisition and preprocessing	46	
50	4.2.1	Data acquisition	46	
50	4.2.2	Image segmentation	47	
50	4.2.3	Image registration	48	
55	4.3	Breast geometry and Finite Elements Mesh	50	
55	4.4	Breast stress-free geometry	52	
55	4.5	Boundary conditions	53	
55	4.6	Materials constitutive models	54	
60	5	Model validation	57	
60	5.1	Technical approach	57	
60	5.2	Results	57	
60	5.3	Discussions and conclusion	60	
65	III	Breast Compression: a comparative study		61
65	6	Background		62
65	6.1	Introduction		62

6.2	Breast compression: overview	62
6.3	Compression paddle designs	62
6.4	Discussions and Conclusion	63
70	7 Breast compression quality evaluation 	64
71	7.1 Compression paddles FE models	64
72	7.2 Compresure quality metrics	64
73	7.2.1 Patient comfort	64
74	7.2.2 Image quality	64
75	7.2.3 Average glandular dose	65
76	7.3 Results	65
77	7.4 Discussions and conclusion	70
IV	Thesis review 	71
80	8 General conclusion and perspectives 	72
81	8.1 Conclusion	72
82	8.2 Perspectives	72
	Bibliography	73

List of Figures

85	2.1	Breast embryogenesis: embryonic evolution of duct system. The epidermis is responsible for the creation of ductal system and alveoli, the dermis mesenchyme is responsible for the creation of connective tissue and vessels	4
90	2.2	Breast development sequence into subcutaneous tissues. A Mammary bud development by splitting the superficial fascia in 2 layers. B Mammary bud development by superficial fascia retracting	5
95	2.3	Left: thorax landmarks; Right: four breast quadrants	6
	2.4	Breast anatomy	7
	2.5	Skin anatomy	8
	2.6	Suspensory ligaments	9
	2.7	Lymphatic system and Mammary Arteries for adult female breast	10
	2.8	Mammographyc exam	13
100	3.5	a) Lagrangian mesh formulation. b) Euler mesh formulation	29
	3.6	From strong formulation of the generalized momentum balance to numerical equations.	29
	3.7	a) Discretization of a 2D domain with triangular finite elements :Lagrangian mesh . b) Different types of finite elements	30
	3.8	Computation of aspect ratio for a triangle	31
	3.9	Example of triangles with different maximal corner angles.	31
	3.10	Example of triangles with different skewness.	32
	3.11	Multi-body contact problem.	33
105	3.12	Contact status update using a pinball of radius r.	35
	3.13	a) Body \mathcal{A} and body \mathcal{B} are close but not in contact. The $d_1(x_B, \mathcal{A})$ measure define the gap between the bodies at point x_B . b) Body \mathcal{B} have penetrated the body \mathcal{A} . The $d_1(x_B, \mathcal{A})$ measure gives the penetration at point x_B	36
110	3.14	The contact surface projection over the target surface: a) Target discretized area; b) contact discretized area; c) intersection of the projected surfaces.	36
	3.15	Prediction-correction algorithm	39
	4.1	MRI images in three breast configuration: first line- subject 1; second line- subject 2	47

LIST OF FIGURES

115	4.2 Breast tissues segmentation on the breast MRI of the second subject. Prone breast configuration. White-voxel belongs to breast tissue; blue - voxel don't belongs to fatty tissue	48
120	4.3 Registered MRI images: first line- subject 1; second line- subject 2; first column - prone configuration versus supine; second column - supine tilted versus supine	49
125	4.4 Anatomical planes and nominal Cartesian axis directions.	50
130	4.5 3D geometries generation. a) MR images; b) segmeted image; c) corresponding 3D geometries	51
135	4.6 Finite elements mesh components. The tissues components are cropped for visualization purposes.	51
140	4.7 Finite elements mesh quality.	52
145	4.8 Fixed point type iterative algorithm for stress-free geometry approximation. D_i - mean node to node distance over the active nodes at iteration i , G - gravity force	53
150	4.9 Finite elements mesh boundaries	54
155	4.10 First column: relation between maximal and mean nodes displacement and the equivalent Young's modulus variation for different tissues. Second column: rate and cumulative change rate of node displacement in function of quivalent Young's modulus	56
160	5.1 Process to estimate optimal material parameters	57
165	5.2 Hausdorff distance on the skin surface over the constitutive parameters space	58
170	5.3 Three breast configurations: prone, supine and supine tilted. First line - MR images in 3 breast configurations. Second and third lines - point to node distance from simulated breast shape (surface mesh) to the measured one (black grid lines).	59
175	6.1 Breast compression between the paddle (up) and the receiver (down): a) Rigid paddle; b)Flex paddle with flexion angle α	63
180	7.1 Microclcification distribution over the smallest breast volume ($d = 10mm$): a)axial view, b) sagittal view.	65
185	7.2 Resulting breast thickness for a given compression force	65
190	7.3 Stress, strain and contact pressure distribution for the first subject	67
195	7.4 Stress, strain and contact pressure distribution for the second subject	68
200	7.5 Breast nominal thickness (BNT), average glandular dose (AGD), signal-to-noise-ratio (SNR) and signal-difference-to-noise (SDNR) for both volunteers and both compression paddle types	69

List of Tables

3.1	Surface interaction models and behaviors	34
3.2	Material properties for adipose and glandular tissues.	41
3.3	Breast biomechanical models	45
155	4.1 Compression force and breast thickness for both subjects for a cranio-caudal mammogram	47

Introduction

1.1 General Problem statement

1.2 Technical approach

1.3 Thesis overview

1.4 Key contributions

1.5 Software

1.6 Ethics

Part I

Background

Clinical background

2.1 Introduction

170 2.2 Breast anatomy

2.2.1 Breast embryogenesis

The breast is a modified skin gland which start to develop at the embryonic stage from the epidermis and dermis. During the sixth fetal month, **form** 12 to 20 solid cords of epithelial cells are growing down into the dermis (fig. 2.1.a-b). Later, these cords evolve into lactiferous ducts and alveoli (fig. 2.1.c-d). Thus, near birth, a simple network of branching ducts is already developed in the pectoral area (Skandalakis, 2009).

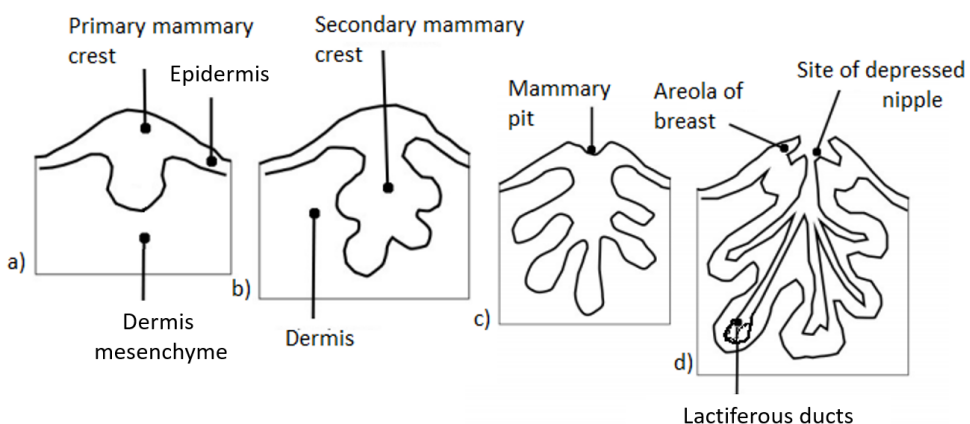


Figure 2.1: Breast embryogenesis: stages of formation pf the duct system. the ectoderm is responsible for duct system and alveoli, the mesenchyme is responsible for the connective tissue and vessels (Skandalakis, 2009).

The glandular **lobes**, generally remain underdeveloped until puberty (13 to 18 years). Under hormonal stimulation, the breast buds due to the development of the mammary glands

and increased deposition of fatty tissues, becoming palpable discs beneath the nipple. The ducts grow into the soft tissues and the lobular differentiation begins (Kopans, 2007).

Kopans (2007) analyzed breast development sequence in the subcutaneous tissues. According to the author the evolution of breast within the fascial system is unclear, with two possible evolution paths:

- 180 1. The superficial fascia split in two layers forming the deep and the superficial fascia layers. The mammary glands forms in between (fig.2.2.A).
- 185 2. The elongating ducts retracts the superficial fascia. The mammary glands is enveloped by the superficial fascia (fig.2.2.B)

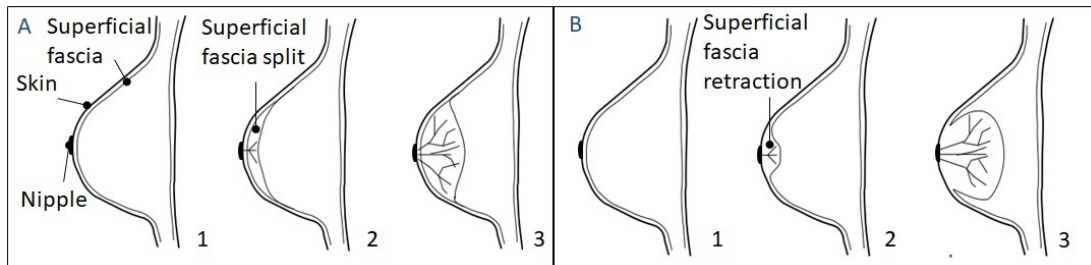


Figure 2.2: Breast development sequence in the subcutaneous tissues. A Mammary bud development by splitting the superficial fascia in 2 layers. B Mammary bud development by fascia retracting, reproduced from (Kopans, 2007)

2.2.2 Breast Appearance

subsection:breastappearance

190 In order to describe the breast appearance, several notions for localization into the breast volume and its vicinity are defined. Usually, the breast volume is divided into four quadrants: upper outer quadrant (UOQ), upper inner quadrant (UIQ), lower outer quadrant (LOQ), lower inner quadrant (LIQ)(see fig.2.3). However, the breast surroundings are localized using the anatomical landmarks as: the inframammary fold, clavicle, sternal angle, sternal line, costal margin and the axilla.

195 Starting with the Warner Brother Corset Company in 1935 the underwear industry introduced a new unit to measure the breast volume, the cup. The cup size is computed using a relation between the circumference of the chest at the level of the nipples and the torso width (Pechter, 1998).

200 Anatomically, the adult breast is localized on top of the ribcage, between the clavicle superiorly and costal margin inferiorly. Its traverse boundaries are defined from the sternal line medially to the midaxillary line laterally (Figure 2.3). The intra-individual asymmetry is considered as a normality for the young and the adult breast (between left and right breast). The breast shape and contour are influenced by (Mugea and Shiffman, 2014):

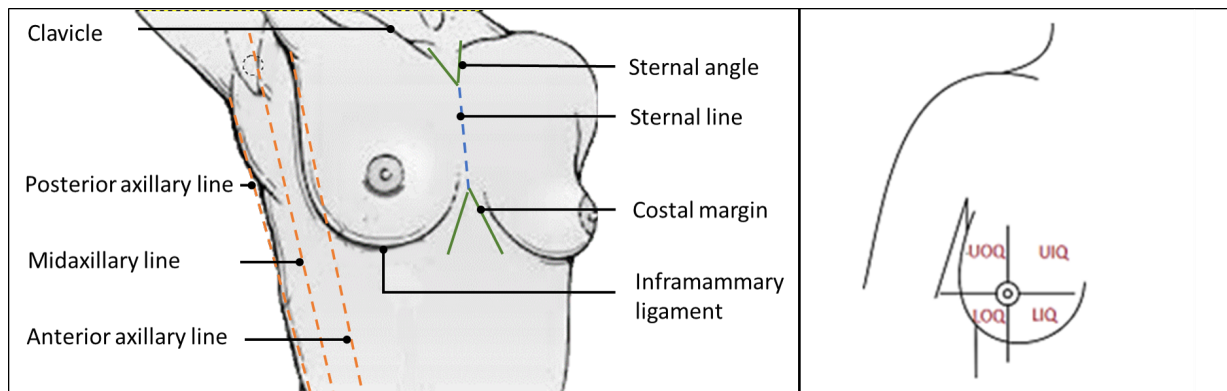


Figure 2.3: Left: thorax landmarks; Right: four breast quadrants

- 205 • The volume of mammary gland in each breast quadrants.
- The amount of the subcutaneous and intra-lobular fat.
- The body contour of the chest wall.
- The muscular covering and thickness.
- The thickness and elasticity of the skin.

210 Anthropomorphic characteristics of women breast were studied almost for the aim of cosmetic and reconstructive surgery. Vandeput and Nelissen (2002) measured distances between anatomical landmarks of the thorax of the 973 women with aesthetically near-perfect breasts. The authors proposed different relations as guidelines to compute the recommended breast size parameters (nipple-mid clavicle distance, nipple inframammary fold distance) as a relation of body parameters (body height, torso width). In their study, a poor correlation was found between body height or weight and breast volume. Contrariwise a high correlation was found between the nipple to **the** inframammary fold distance or the nipple to **the** mid clavicle distance and the thorax width. Catanuto et al. (2008) mentioned that the breast shape after surgery cannot be predicted by volumetric measurements only
215 and have proposed additional measures (**surface, distance** or angles) **permitting to characterize unambiguously** the breast shape. According to authors, the curvature of the thoracic surface is the most relevant parameter to evaluate the outcome of a reconstructive breast surgery.
220

2.2.3 Internal structure

225 Breast heterogeneous structure includes a mixture of parenchyma and adipose tissue (Figure 2.4). The breast parenchyma consists of: glandular components, lymphatic network and blood vessels (Clemente, 2011). Skin, Cooper's ligaments and fascias are the supporting system of the breast, their interconnection and intersections with the pectoral muscle fix and support the breast soft tissues (Mugea and Shiffman, 2014).

²³⁰ **Adipose tissue** is the predominant tissue of the breast that fills up depressions between the deep and superficial fascia. In the intra-fascial space, adipose tissue surrounds and is dispersed among the glandular structures. Fat properties and its spatial distribution **gives** the breast a soft consistency. The main aim of this tissue is to protect the lobes and lactiferous ducts.

²³⁵ **Glandular tissue** is represented by breast lobes. A healthy female breast is made up of 12-20 lobes. They are distributed centrally and laterally within the breast. The total amount of glandular tissue depends on the hormonal fluctuation, age and physical state. Mammary ducts arise from the lobes as branches and connect them to the female nipple. There are about 10 duct systems with a tree-like structure in each breast that carry the milk from the lobes to the nipple. The dark area of skin surrounding the nipple is called the areola. Huang et al. (2011) have studied the breast shape and fibro-glandular distribution using dedicated breast CT images. This study shows that the glandular tissues is situated in the central portion of the breast. In prone position about 60 % of glandular tissues is located near to the nipple. A mean percentage of glandular tissue was computed by Yaffe ²⁴⁰ et al. (2009), the values varied from 13.7% to 25.6 % within different groups. They also mentioned a drop in glandular fraction with the advancing age.

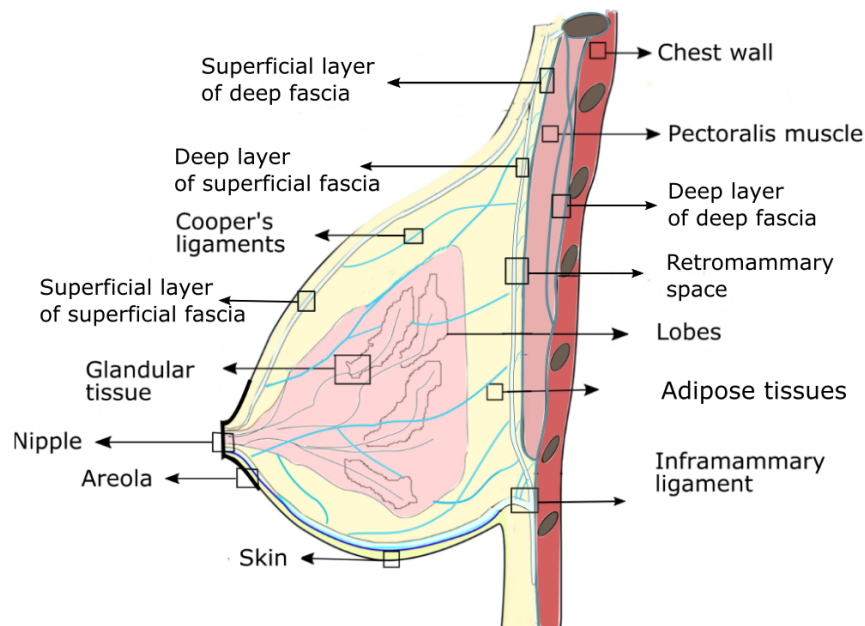


Figure 2.4: Breast anatomy

A layer of adipose tissue and connective fascia separates the breast from the pectoral muscle forming a retro-mammary fat space.

²⁵⁰ The **skin** is the covering breast layer which provides protection and receives sensory stimuli from the external environment. It is a heterogeneous organ composed of 3 layers

(see fig. 2.5 , (Kanitakis, 2002)): epidermis (dead cells) mainly composed of keratin, dermis composed of collagen and elastin fibers in a viscous matrix made of water and glycoproteins and hypodermis, mainly composed of adipocytes cells.

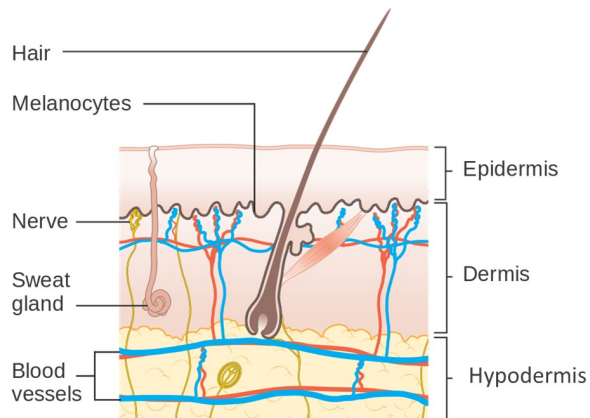


Figure 2.5: Skin anatomy

255 The breast skin thickness **variate** from breast base to the nipple form $\sim 2\text{ mm}$ to $\sim 0.5\text{ mm}$. At the nipple areola region, the skin thickness measure $4\text{-}5\text{ mm}$. (Andolina and Lillé, 2011). Sutradhar and Miller (2013) studied the breast skin thickness of 16 different sectors radially oriented around the nipple. The thickness range proposed by the authors relies between 0.83mm and 2.35mm with a mean of $1.55 \pm 0.04\text{mm}$. According to this study
260 the skin thickness varies as follows: the lateral region thickness is the thinnest among all the breast regions followed by superior/inferior and medial region; there is no significant difference between the inferior and superior breast regions; in the radially exterior region thickness is thicker than the radially interior region thickness (close to the nipple). Ulger et al. (2003) found that, during the breast puberty, **then the breast volume increase**, the
265 skin thickness decreases in all regions.

270 **Connective tissue** is represented by Cooper's ligaments and fascial system. The breast fascial system is composed of deep fascia and superficial fascia. During puberty, breast is growing and superficial fascia divides in two layers: deep and superficial layers (Kopans, 2007). Cooper's ligaments run throughout the breast tissue parenchyma from the deep
275 fascia beneath the breast to the superficial layer of superficial fascia where they are attached (Figure 2.4). Because they are not taut, these ligaments allow the natural motion of the breast (Clemente, 2011). Between the superficial layer of the deep fascia and the deep layer of the superficial fascia, a layer of connective loose tissue forms the retro-mammary space, allowing the breast tissue to glide over the chest (Mugea and Shiffman, 2014). In regions where the superficial fascia meets the deep fascia, suspension ligaments are created. One of these ligaments is situated at the level of the sixth and seventh ribs and is **called inframammary ligament** (Bayati and Seckel, 1995). It evolves into the **deep lateral ligament** and the **deep cranial ligament** that are respectively attached to the axillary

fascia and to the clavicle. Another meeting point of the 2 fascias is situated on the sternal line and is called **deep medial ligament**.²⁸⁰

The existence, the topography, and the thickness of the membranous layers of superficial fascia have been studied in various regions of the body (Abu-Hijleh et al., 2006). According to the authors, the thickness of the superficial layer in both superior and inferior breast regions is equal to $88.12 \pm 7.70\mu m$ and $140.27 \pm 11.03\mu m$ respectively.

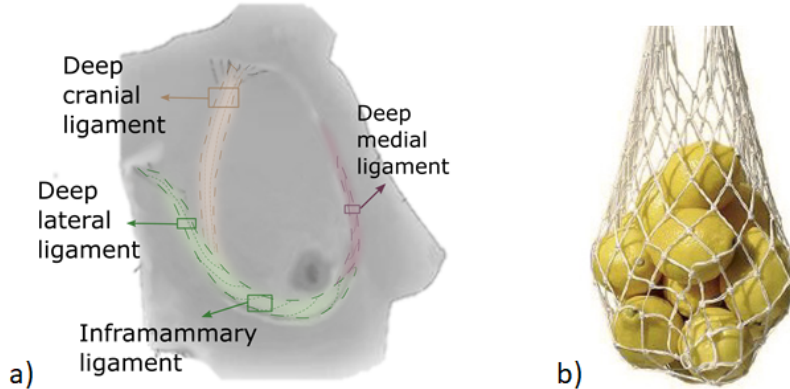


Figure 2.6: **Suspensory ligaments**

²⁸⁵ The lymphatic system is a vessel network which insures the transportation of white blood cells from tissues into the bloodstream. The majority of intramammary nodes are associated with the upper outer breast tissue and the lower outer part of the breast (Kopans, 2007). All intramammary lymph nodes are in the lateral half of the breast along the margin of the breast parenchyma. Lymphatic drainage of breast extends from the ²⁹⁰ subareolar plexus deep to and around the nipple (Figure 2.7).

The blood supply from the breast comes primarily from the internal mammary artery named successively subclavian, axillary, and brachial artery (Figure 2.7), from which lateral and internal thoracic artery runs underneath the main breast tissue.

2.2.4 Adult breast texture changes

²⁹⁵ The female breast undergoes substantial changes during the lifetime. The main part of them is caused by hormones and by woman's physiological condition. Important changes in female breast stiffness and composition occur during the menstrual cycle, pregnancy and menopause.

³⁰⁰ There are 3 important changes during the menstrual cycle caused by hormonal changes (Andolina and Lillé, 2011). During the first phase the estrogen (female hormones) diffusion stimulates epithelial cell multiplication and enlargement of ductal structures. Next, during ovulation epithelial cell begin to grow in the lobule due to progesterone hormones, an increase in blood flow is also noticed. In the last phase, the ductal structures and lobes support an involution and regression process. It must be mentioned that not all lobules

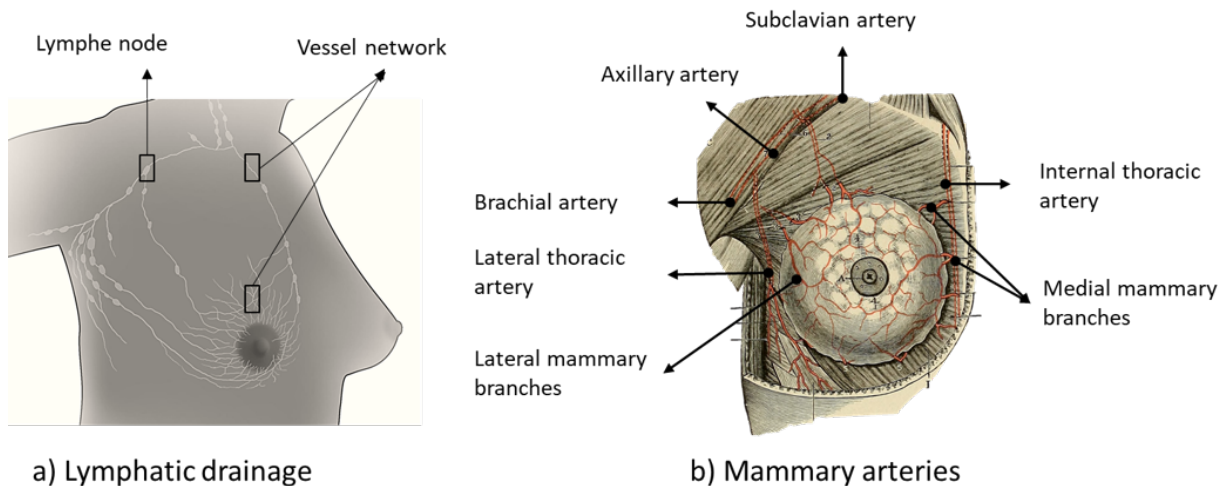


Figure 2.7: Lymphatic system and Mammary Arteries for adult female breast

305 regress, therefore during menstrual cycle new lobules can be created. The work by Lorenzen et al. (2003) showed that during the premenstrual phase the stiffness of fibro-glandular tissue and glandular tissue can change by 30% and 14 % respectively. They also show that in the middle of the menstrual cycle, the parenchyma volume increases of 38% and the water content by 24.5%. **A**

310 During the pregnancy under the influence of estrogen and progesterone the breast enlarges in volume and density, the veins dilate and the **ratio** of parenchyma tissues increases. When lactation is weaned, and the glandular, ductal, and stromal elements atrophy resulting in decrease in breast size (Pandya and Moore, 2011).

315 The menopausal breast contains a larger fraction of fatty tissues and reduce the number of ductal and lobular elements. During the first four years after menopause the breast is the subject of an atrophy process. The atrophy begins medially and posteriorly, then laterally, working its way to the nipple (Andolina and Lillé, 2011). In this period the breast loses progressively fat and stoma **tissues** resulting in breast shrinkage and loss **off** contours.

320 The breast support matrix can be stretched and attenuated by weight changes occurred during the pregnancy and can relax with aging. The different changes can result in excess breast mobility over the chest and ptosis.

2.3 Breast Cancer

The first written description of breast cancer was on ancient Egyptian papyrus. At that time the treatment was considered futile and the woman was left without any medical assistance. Ancient Greeks, thought that the breast cancer was caused by an excess of black bile. It was thought that the monthly menstrual flow naturally relieved women of this excess, which explained why breast cancer was more common after menopause (Andolina and Lillé, 2011).

Nowadays, several research (Pike et al., 1993; Martin, 2017) have shown that the cancer 330 is always caused by damages to a cell's DNA. The initiation of the mutagenic process that may results in various genetic errors require the cell division. A factor that increase 335 cell proliferation will increase also the risk of cancer. The woman hormones, estrogen and progesterone, appear to impact the breast cell division rate (Ciocca and Fanelli, 1997; Fanelli et al., 1996), which explain the high rates of breast cancer in women (more than 345 99% of breast cancer occurs in women). The risks of developing a cancer is increased by various factors like age, genetics, family history or life style. According to (Martin, 2017) the breast cancer risk factors can be explained by woman exposure to the ovarian hormones during her lifetime.

The breast cancer is the second most frequent type of cancer and is the leading cause 340 of death within women with cancer diagnostic (SPF, 2016). The Foundation for Medical Research (FRM, 2017) estimates the risk of developing breast cancer for french women as 1 in 8 with more than 47% of cases diagnosed on women within 65 years old. After the French Public Health Agency SPF (2016) the incidence of breast cancer has increased by 138% between 1980 and 2005. In United Kingdom and United States by the year 2000 345 the death rate from breast cancer had declined by almost 20% and in 2005 was down by 25% (Peto et al., 2000). This significant improvement was attributable to rise in the life expectancy and the upgrowth of screening technologies.

2.3.1 Cancer classification

The breast cancer type is determined by the specific cells that are affected. When a woman 350 is developing a breast cancer, more frequently the primary tumor is developed in the epithelial cells, this type of tumor is called carcinomas. The primary tumor can also start in cell from other tissues as muscle, fat or connective tissues. These types of tumors are called sarcomas, phyllodes, Paget disease and angiosarcomas but they are much rarer ACS 355 (2017).

The carcinomas are then classified based on their location and how far the cancerous cell have spread. Then the cancerous cells remain within the milk ducts or lobules, the cancer is classified as non-invasive cancer. Otherwise, then the malignant cancerous cells break through normal breast tissue barriers and spread out through other body organs, they are classified as invasive cancer (Andolina and Lillé, 2011). The most common types 360 of carcinomas characterized by their location are: ductal carcinoma and lobular carcinoma.

The invasive ductal carcinoma starts in the epithelial cells that line the milk ducts, whereas the invasive lobular carcinoma starts in the lobules. Both evolve through the surrounding tissues and may widespread to the other organs through the bloodstream and lymph nodes (metastasize).

Although the non-invasive carcinomas are not malignant, it has a 40% chance to change to an invasive carcinoma over a 30-year period. The non-invasive ductal carcinoma starts and stay inside the milk duct. The non-invasive lobular carcinoma overgrowth the normal breast cells and stay inside the lobule.

Invasive lobular carcinoma may be harder to detect on physical exam as well as imaging, like mammograms, than invasive ductal carcinoma. And compared to other kinds of invasive carcinoma, about 1 in 5 women with ILC might have cancer in both breasts. Non-invasive ductal carcinoma is the more commonly detected form, making up 4% of symptomatic cancer and 20% of the cancer detected during a screening program. Its presence may be indicated on X-ray mammogram by microcalcifications (ACS, 2017).

375 2.3.2 Breast cancer screening

subsection:cancerscreening Early detection remains the primary defense available to prevent the development of breast cancer. The early detection consists of regular screening test aimed to find breast cancer before any symptoms can develop. The principal benefit of the regular screening is the potential to prevent the premature and often prolonged, 380 painful death of the individual. Studies have shown that regular mammographic screening resulted in a 63% reduction in breast carcinoma death among women who actually underwent screening (Tabár et al., 2001). In 2012, the review of the UK screening program (NHSBSP, 2012) showed that it prevented 1300 deaths from breast cancer a year.

Secondary benefits include a reduction in the trauma of treating earlier-stage lesions. 385 Earlier found invasive carcinoma respond better to treatment which means that the patient may avoid having a mastectomy or a chemotherapy.

Various worldwide countries have adopted organized breast screening examination programs. Depending on the regional statistics and the estimated risk factors (age group, 390 breast density, family history etc) the population is invited to participate to a free screening examination. In 1994, the French National Authority for Health approved a national screening program (FNAH, 2016). Since then, every woman within 50 and 74 years old, is invited one in two years for a clinical exam and a mammography.

The individuals who are suspected of having breast cancer, will have additional diagnostic tests as : diagnostic mammography, ultrasound, MRI, biopsy, blood test etc. The 395 diagnostic test help not only to confirm or not the screening results, but also, in case of positive test, to determine the stage and the type of the breast cancer.

2.4 Medical Imaging

2.4.1 X-ray mammography

X-ray mammography is a type of medical imaging that uses x-rays to capture images 400 of the internal structures of the breast (FDA definition). In digital mammography (also known as Full Field Digital Mammography, FFDM) x-rays are beamed through the breast to an image receptor (Figure 2.8). A scanner converts x-ray to digital information. The mammography can be used to detect parenchymal distortion, asymmetry, masses and microcalcifications within the breast.

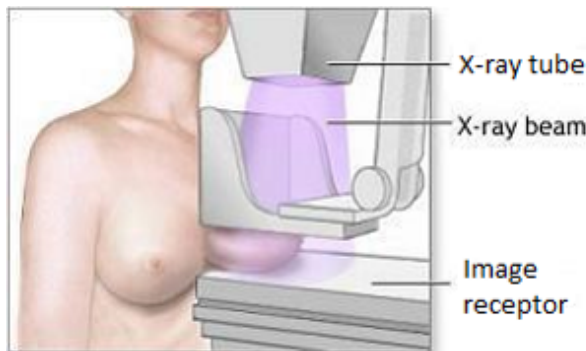


Figure 2.8: Mammographyc exam

405 A standard mammographic protocol always includes breast compression prior to image acquisition. Women breast is compressed between two plates until a nearly uniform breast thickness is obtained. Nowadays, the European Commission recommends a force standardized breast compression, i.e. the compression stops at a level of force just below the subjects pain threshold or to the maximum setting of the machine (not to exceed 200 N).
 410 Modern mammographic systems used fin films to display breast internal structures, thus the compression was needed in order to assure a uniform exposure over the breast volume. With digital mammography systems, the exposure variation could be corrected, however the breast compression is still indispensable for the next reasons: to hold the breast away from the chest wall; to reduce the blur due to physical motion; to reduce the absorbed dose
 415 of ionizing photons; to separate overlapping structures; to reduce image degrading scatter; to press breast structures closer to the detector (Kopans, 2007).

Screening mammography typically involves taking two views of the breast, from above (cranial-caudal view, CC) and from an oblique or angled view (mediolateral-oblique, MLO). The two views are complementary. The MLO view covers more tissue and provide better
 420 visualization of the upper juxtathoracic part of the breast. While the CC-view suffers less from overlapping dense tissues and provide a better visualization on the central part of the breast (Chan et al., 1987). Further compression or magnified view may be needed for diagnostic mammography.

Studies for different countries have assessed mammography sensitivity and specificity,
 425 the obtained sensitivity range between 81 and 88 %, and the specificity between 90 and 98 % (Kemp Jacobsen et al., 2015; Hofvind et al., 2012). The mammography sensitivity is mostly affected by the dense breasts. A dense breast is a breast which proportion of the fibroglandular tissues exceed greatly the one of fatty tissues. Fatty tissues are radiographically translucent, high intensity signal appear on the mammographic images as
 430 dark areas. Meanwhile, the fibroglandular tissues and breast cancers tend to absorb the x-rays photons, therefore they will appear as white areas. The lack of contrast between the cancer and background on white areas will make the detection mode difficult.

2.4.2 Ultrasounds

Breast ultrasound uses high-frequency sound waves to make image of the breast inside tissues. The ultrasound technician put gel on the skin above the area of interest and moves the sound-emitting probe over the skin. The emitted waves are bounced by the breast soft tissues. The probe picks up the resulting waves and transformed them into a 2D images.

For asymptomatic women, a careful investigation of lateral and profound breast tissues is needed to identify the suspicious legions. The limited field of view of the ultrasound image prevent from seeing abnormalities that lie deeper in the breast. Consequently, the ultrasounds are not sufficient for regular screening and are used to complement other screening tests. However, it is widely used to investigate suspicious legions found within mammography, clinical or self-examinations. The ultrasound is particularly effective in differentiating between cysts and cancers, but have a low sensitivity for microcalcification detection which are the most common feature of tissue around a tumor. The ultrasound can also be used for differential diagnosis, local staging and interventions guidance.

The ultrasound elastography is a sonographic imaging technique combining the ultrasound technology with the basic physical principles of elastography. Elastography assesses tissue deformability by providing information on the tissues elasticity, it consists of either an image of strain in response to force or an image of estimated elastic modulus. It's a equivalent method to clinical or self-examination with higher precision.

The shear-wave elastography (SWE) use a focused pulse of ultrasound generated by the probe to induce soft tissues deformation. The tissues elasticity is assessed either by directly measuring soft tissues deformation or by measuring the speed of shear wave propagation. The combination of SWE with conventional ultrasound increases the diagnostic performance for breast lesions, compared with conventional ultrasound alone (Youk et al., 2017). The elastography serve as a complementary tool to differentiate between benign and malignant lesions by providing information about the lesion stiffness(Itoh et al., 2006; Olgun et al., 2014)

2.4.3 Magnetic resonance imaging

Magnetic resonance imaging is a noninvasive procedure for studying internal structure of the body that cannot be properly seen through normal X-rays (example: dense breasts). It employs radio-frequency(RF) waves and intense magnetic fields to excite hydrogen atoms. Body parts that contain hydrogen atoms (e.g. in water) are thus visible within fine details. The quality of the image produced by MRI techniques depends, in part, on the strength of the received signal. For higher image quality, it is optimal to use an independent RF receiving coil placed in close proximity to the region of interest. For breast imaging a dedicated breast MRI coils is used. The patient is placed in prone position with the breast inside the coil and both arms by the sides of the body.

For breast cancer imaging, a contrast agent is employed to enhance highly vascularized regions. Then the cancerous tumor develops, new vascularizations are created on the

direct surrounding to provide oxygen. Thus, the lesions are visualized due to their uptake of contrast agent. The contrast enhanced MRI are used as screening modality for woman with high risk of cancer.

Low specificity and high cost of MRI restricted its use in routine screening (Peters et al., 2008), however it is increasingly used for high-risk groups and for lesions that are difficult to detect with mammography or ultrasounds tests.

2.5 Conclusion

Today, mammography is the by far primary imaging modality for breast cancer screening and plays an important role in cancer diagnostics. The number of mammography exams per year was estimated at 150 million which corresponds to almost 80 images per second during working hours. Ultrasound (U/S) and Magnetic Resonance Imaging (MRI) are complementary imaging techniques used mostly for dense breasts and high-risk women.

However, the discomfort and pain produced by this procedure sometimes might deter women from attending breast screening by mammography (Aro et al., 1999; Fleming et al., 2013). In a study by (Dullum et al., 2000) more than 50% of attendants (N= 1800) mentioned from moderate to extreme physical discomfort. It has been reported that the fear for pain itself can already be a reason to avoid getting the first mammogram (Andrews, 2001), and that 15% of those who skipped the second appointment cited as the main cause an unpleasant or painful first mammogram (Fleming et al., 2013; Whelehan et al., 2013).

The direct cause of pain in mammography is the flattening of the breast which is directly linked to the applied compression force. Latest researches indicate that with a reduced level of compression (10N vs 30N), 24% of women did not experience a difference in breast thickness. If breast thickness is not reduced when compression force is applied, then discomfort is increased with no benefit in image quality or mean average dose.

Therefore, there is an opportunity to leverage the potential of the recent imaging technologies to investigate alternative breast compression techniques, considering the patient comfort in addition to an improved image quality and a reduced ionizing radiation dose. The aim of this work is to compare the physical comfort when the breasts are compressed using different designs of compression paddles, and to identify the best compression paddle that may help improving the patient comfort and therefore the adherence to breast cancer screening.

In this scope a biomechanical Finite Element (FE) breast model is developed and evaluated on real deformation measured on MR images. The tissues internal stress/strain intensities are used as a first estimate of the physical comfort. The deformed geometry is the subject of a Monte-Carlo image simulation allowing to assess the Image Quality (IQ) and Average Glandular Dose (AGD).

Part II

Biomechanical breast modeling

Background and state of the art

3.1 Introduction

3.2 Continuous mechanics

515 3.2.1 Deformation and strain

ontinuous mechanics is the mathematical description of how objects that occur in nature respond to the application of forces or other external stimuli.

A **body** is the mathematical abstraction of an "object" and is defined by its geometric and constitutive character. In a macroscopic appearance, a solid "object" is described as homogeneous and continuous "body", i.e. the substance of the object have a unique composition and completely fills the space it occupies ignoring the granular (atomic) nature of matter. In continuous mechanics, a body \mathcal{B} is composed of a set of **particles** p (or material points). Each particle is located at some definite **point** x in three dimensional space. The set of all the points in space, corresponding to the locations of all the particles, is the **domain** Ω occupied by the body in a given configuration, here also named *geometry*. A particular body can change it's configuration and therefore the occupied region in the space then exposed to some external stimuli like force, pressure or heat.

The **configuration** of a body is defined as a one-to-one mapping between the particle p and position x , $\Omega_0 = \chi_0(\mathcal{B})$ (see figure 3.1). To describe solid's respond to an external stimuli one needs to know the changes in geometrical characteristics between at least two configurations: the configuration that one wishes to analyze Ω_1 , and the **reference configuration** relative to which the changes are to be measured Ω_0 . Here, see figure 3.1, the mappings χ_0 and χ_1 take $p \rightarrow X$ and $p \rightarrow x$, thus X and x are the positions of particle p in the two configurations under consideration.

535 Frequently, the reference configuration is fixed for a given study and is chosen arbitrary in a the most convenient way among all the configurations that the body can sustain.

The **deformation** of the body from the reference configuration Ω_0 is characterized by the next defined mapping Φ :

$$x = \Phi(X) = \chi_1(\chi_0^{-1}(X)), \quad \text{where } X \in \Omega_0 \text{ and } x \in \Omega_1 \quad (3.1)$$

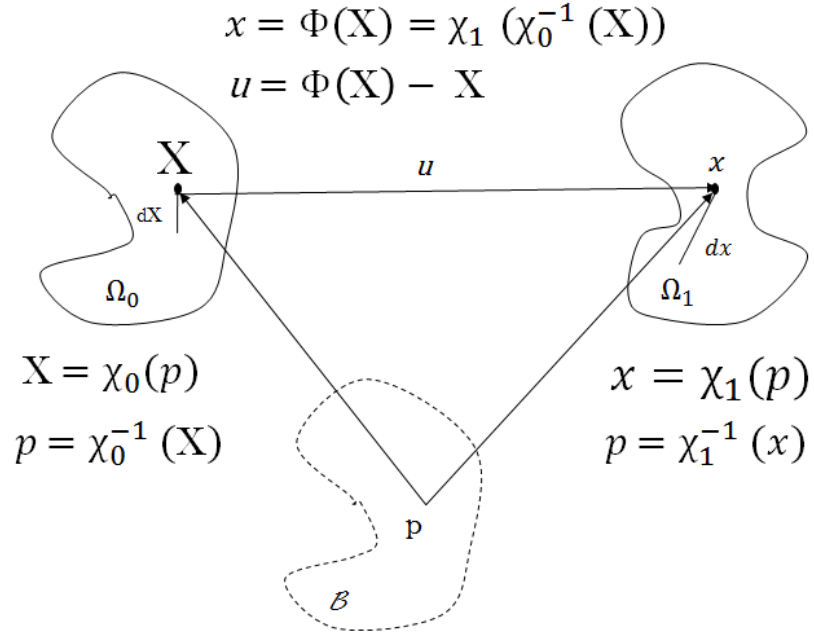


Figure 3.1

The **displacement** u of a particle is the difference between its position in the analyzed configuration (or current configuration) and its position in the reference configuration.

$$u(X) = \Phi(X) - X \quad (3.2)$$

Suppose that $G(\Omega_1)$ is the value of some extensive physical property associated with the body β in the current configuration (such as the body mass m). There exists a density $g(x)$ such that:

$$G(\Omega_1) = \int_{\Omega_1} g(x) dv$$

where dv is the volume of the material element. Thus, the property $G(\Omega_1)$ is related to the body and the density $g(x)$ is related to the position of the body particle.

Eulerian and Lagrangian formulations

There are two classical techniques used to describe the body physical characteristics depending on the choice of independent variables. Some physical characteristics, such as mass density, can be defined for each individual particle. In such cases, the body characteristics are defined by the function

$$m = \mathcal{M}(p)$$

for all $p \in \mathcal{B}$. Here the coordinate system remains consistent and move with the particle. Therefore, the coordinates of both, the particle and the attached variable do not change

along the deformation. Since a particle is an abstract entity it cannot be used in numerical calculations therefore the particle is described by its location in reference configuration $p = \chi_0^{-1}(X)$.

$$m = \mathcal{M}(p) = \mathcal{M}(\chi_0^{-1}(X))$$

We call X Lagrangian or material coordinates and their application is called Lagrangian or material description.
545

Instead of defining body characteristics as a function of body particles, one can define it directly as a function of particle location in current configuration by using the relation $x = \chi_1(p)$, and therefore

$$m = \tilde{\mathcal{M}}(x) = \mathcal{M}(\chi_1^{-1}(x))$$

Here the coordinate system is fixed and the particles coordinate are changing. Therefore, the position of particle and any related quantity changes during the deformation. We call x Eulerian or spatial coordinates and their application is called Eulerian or spatial description.

550 These approaches are distinguished by three important aspects: the mesh description, the stress tensor and momentum equilibrium and the strain measure. The advantages and drawback of two formulations will be discussed later in this chapter. Further, only Lagrangian formulation is used to describe the continuous deformation of soft tissues.

Deformation gradient

555 In mathematical formulation the deformation gradient F is the Jacobian matrix of the deformation $\Phi(X)$:

$$F = \frac{\partial \Phi(X)}{\partial X} = \frac{\partial x}{\partial X} \quad (3.3)$$

Considering infinitesimal quantities, the deformation gradient relates the segment dX in the reference configuration to the corresponding deformed segment dx in the current configuration (Figure 3.1)

$$dx = F \cdot dX. \quad (3.4)$$

560 In addition to the mapping line elements, the deformation gradient tensor allows also the mapping of differential volumes as:

$$dv = \det(F)dV = JdV \quad (3.5)$$

The Jacobian determinant of the deformation gradient tensor J is a measure of the volume variation during the deformation. The Jacobian determinant can be used to relate extensive physical properties in the current and reference configurations by the next
565 equality:

$$\int_{\Omega_1} g(x)dv = \int_{\Omega_0} g(\Phi(X))JdV \quad (3.6)$$

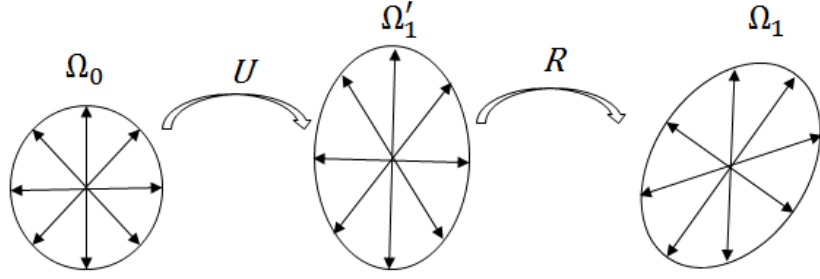


Figure 3.2: Decomposition by rotation and a stretch of a material particle.

Decomposition of deformation gradient tensor into rotation and stretch

The deformation gradient tensor represents the entire body deformation, which consist of rigid body rotation and body "stretch" (see fig. 3.2). As dX and dx are differential segments, the map F is not affected by rigid-body translations. Generally, the body stretch is defined as the ratio of the deformed line elements to the length of the corresponding undeformed line element:

$$\hat{\lambda} = \frac{|dx|}{|dX|} \quad (3.7)$$

Using polar decomposition theorem, the deformation tensor can be written as the product of a proper orthogonal tensor R representing the rotational part, and a symmetric positive defined tensor U representing the body distortion.

$$F = R \cdot U. \quad (3.8)$$

where U and R are given by the relations $U = (F^T \cdot F)^{\frac{1}{2}}$ and $R = F \cdot U^{-1}$. The tensor U is also called the **right stretch tensor**. Since there is a one-to-one relation between U and U^2 , for the simplification of numerical calculus the stretch tensor can be replaced by the **Green deformation tensor** $C = F^T \cdot F$.

Where are three particular functions of C called the principal scalar invariants.

$$I_1(C) = \text{tr}C, \quad I_2(C) = \frac{1}{2} [\text{tr}C^2 - (\text{tr}C)^2], \quad I_3(C) = \det(C) \quad (3.9)$$

The interpretation is that, the body "stretch" consists (locally) of three mutually orthogonal stretches, "the principal stretches". The latter are scalar combinations of C components that do not change under coordinate transformations for a given body configuration. The use of invariants will be an essential part of constitutive modeling, because the behavior of a material should not depend on the coordinate system.

It can be also shown that:

$$\det(C - \mu I) = -\mu^3 + I_1(C)\mu^2 - I_2(C)\mu + I_3(C) \quad (3.10)$$

Strain measures

Referring to small deformations, the engineering nominal strain is defined as the ratio of the change in length of the deformed line element to the length of the corresponding undeformed line element:

$$\epsilon = \frac{dx - dX}{dX} \quad (3.11)$$

Then the body is not deformed, the deformation gradient F and therefore the right stretch tensor U is equal to identity tensor I . The strain in such case is equal to zero.

Then one is modeling biological soft tissues, large deformation have to be considered. Therefore, the previously defined strain is no more applicable. For large deformations, a measure of strain can be any monotonically increasing function related to stretch in a one-to-one manner and what completely vanishes in the reference configuration.

In orthogonal coordinate system, an admissible function is:

$$f(x) = \frac{1}{m}(x^m - 1) \quad (m \neq 0) \quad \text{and} \quad \ln(x) \quad (m = 0) \quad (3.12)$$

Then $m = 2$ the function is named the Green-Lagrangian stain tensor:

$$E = \frac{1}{2}(U^2 - I) = \frac{1}{2}(C - I) \quad (3.13)$$

The Green-Lagrangian tensor is commonly used in practice as it can be computed without prior knowledge of the eigenvectors of Green deformation tensor C .

3.2.2 Stress measures

Body and contact forces

Generally, forces are categorized as internal and external forces. An **external force** is a force caused by an external agent outside of the system, and contrariwise an **internal force** is a force exchanged by the particle in the system. The external forces, in turn, are categorized in **body forces** (acting at the distance) and **contact forces** (acting on the body surface). The relation between body forces per unit undeformed volume $\tilde{b}(X)$ (Lagrangian coordinates) and body forces per unit deformed volume $b(x)$ is given by the following relation:

$$\tilde{b} = \frac{dv}{dV} b = Jb. \quad (3.14)$$

The contact forces can act on the external surface of the body or on a imaginary internal surface enclosing a volume element (Fig. 3.3). In general terms, the stress (or the **traction vector**) $t^n(x)$ is defined as contact force per unit area da in the limit as $da \rightarrow 0$. Therefore $t^n(x)$ varies from point to point in intensity and orientation depending on the $da(n)$ orientation. The stress vector projection on normal axis n define the **normal stress vector** and it's projection on the tangential axis define the **shear stress vector**.

The stress on the boundary $\partial\Omega_1$ of the region occupied by the studied body is applied by external forces through physical contact along the boundary. When formulating and solving a boundary-value problem, this stress define the boundary conditions.

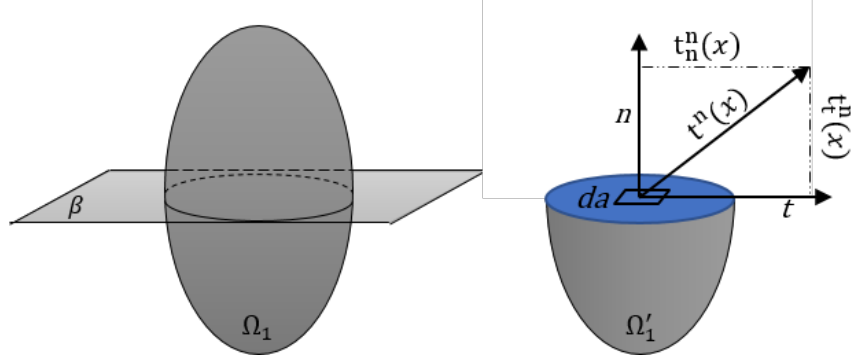


Figure 3.3: True stress vector $t^n(x)$ at point x on the fictitious surface created by the cutting plane β of normal \vec{n} passing through the point x .

Cauchy's lemma

Cauchy's lemma states that traction vectors acting on opposite sides of a surface are equal and opposite.

$$t^{-n}(x) = -t^n(x) \quad (3.15)$$

Cauchy's Law

Cauchy's law states that there exists a Cauchy stress tensor σ which maps linearly the normal to a surface to the stress vector acting on that surface, according to the next relation

$$t^n = \sigma \cdot n \quad \text{where} \quad t_i^n = \sigma_{i,j} n_j \quad (3.16)$$

Then large deformations are considered, the reference and current configurations of the body are significantly different and a clear distinction has to be made between them. The traction vector t^n is defined in Eulerian coordinates (body current configuration) and is also called the **true stress**. Accordingly, the Cauchy stress tensor σ is called the true stress tensor.

The definition of any measure with respect to the deformed configuration is less practical as the current configuration is usually unknown a priori. For the simplification of mathematical formulation, a new pseudostress is defined in the Lagrangian coordinate space named **engineering stress**. The engineering stress have no physical meaning and have to be converted in to true stress for any interpretations.

Next, two pseudostress vectors are defined (Fig. 3.4):

- the contact force df per unit area in reference configuration dA .
- the contact pseudoforce \tilde{df} per unit area in reference configuration dA .

Accordingly, two pseudostress tensors are defined based on pseudostress vectors:

- $T^N = P \cdot N$, P is called **first Piola-Kirchhoff stress tensor**,

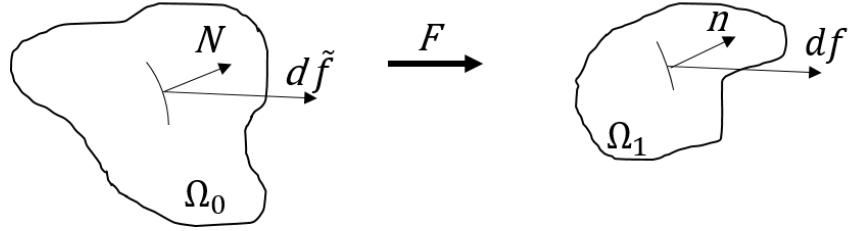


Figure 3.4: Deformation of area dA into area da . The force df acting on deformed area da and the pseudoforce $d\tilde{f}$ acting on undeformed area dA

- 640 • $\tilde{T}^N = S \cdot N$, S is called **second Piola-Kirchhoff stress tensor**.

The three stress tensors are linked by the next relation

$$\sigma = J^{-1}F \cdot P = J^{-1}F \cdot S \cdot F^T \quad (3.17)$$

3.2.3 Conservation equations

Three conservation laws must be satisfied by physical system subject to any applied boundary conditions: **conservation of mass**, **conservation of linear momentum** and **conservation of angular momentum**. The resulting equations describe partially the mechanical behavior of a continuous body.

Conservation of mass

The mass m of a body with the density ρ , that infill the space region Ω_1 is given by :

$$m(\Omega) = \int_{\Omega} \rho(X) dV \quad (3.18)$$

The mass conservation law requires that the body mass remain constant throughout all possible body configurations. For a Lagrangian formulation, this results in a relation between the body density in the reference configuration ρ_1 and the body density in the current configuration ρ .

$$\int_{\Omega_1} \rho_1 dv = \int_{\Omega_0} \rho_0 dV = const.$$

Using the relation 3.6 one can deduce that:

$$\int_{\Omega_0} (\rho_1 J - \rho_0) dv = 0 \quad and \quad \rho_1 J = \rho_0 \quad (3.19)$$

650 **Conservation of the linear momentum**

Assume that a body β defined on a arbitrary region Ω_1 with boundary Γ_1 is subjected to a body-force ρb and the surface traction $a t^n$. And let X be the particle location in the deformed solid. The total force acting on the body β is defined as:

$$f = \int_{\Omega_0} \rho_0 b(X) dV + \int_{\Gamma_0} T^N(X) dA \quad (3.20)$$

The conservation of the linear momentum requires that the total forces acting on the 655 body to be equal to the time rate change of the linear momentum. In a static problem the time rate change of the linear momentum is neglected and thus the next equilibrium equation is obtained.

$$\rho_0 b + \nabla_0 \cdot P = 0 \quad (3.21)$$

here the P_{ji} are the components of first Piola-Kirchhoff stress tensor The equilibrium equation can be formulated in therms of the second Piola-Kirchhoff stress tensor by using 3.17 660 relations.

Conservation of angular momentum

The conservation of angular momentum requires that the resultant momentum on any part of the body about a fixed point \mathcal{O} equals the rate of increasing of its angular momentum (about \mathcal{O}). For a static problem, the integral form of the conservation of angular 665 momentum is defined as:

$$\int_{\Omega_0} X \times \rho_0 b(X) dV + \int_{\partial\Omega_0} X \times T^N(X) dA = 0 \quad (3.22)$$

The relation 3.22 demands that the second Piola-Kirchhoff stress tensor by a symmetric tensor:

$$S = S^T \quad (3.23)$$

In summary, the conservation equations are fulfilled if and only if the following local conditions are fulfilled at each point in the body:

$$\rho_1 J = \rho_0, \quad \nabla_0 \cdot S \cdot F^T + \rho_0 b = 0, \quad S = S^T \quad (3.24)$$

670 with the traction on the surface related to the stress through $\tilde{T}^n = S \cdot N$. For the simplification of mathematical calculus, the constitutive equations are formulated in therms of the second Piola-Kirchhoff stress tensor using the relations 3.17.

3.2.4 Constitutive models

he constitutive models, called also material models, define the relation between stress and 675 strain of a physical system under the action of external stimuli. It is very complex to define a universal material behavior capable to model the material response to all possible

conditions. Thus, for one material, several constitutive models can be defined depending on the studied characteristics.

Based on different characteristics biological materials are classified into:

Isotropic or anisotropic materials: the response of a isotropic (anisotropic) material to an applied load is independent (dependent) of the direction of loading.

Compressible or incompressible materials: in a compressible (incompressible) material the volume is changed (unchanged) during the deformation and the density remains constant. For a incompressible material the Jacobian determinant of the deformation tensor J is equal to 1.

Homogeneous or heterogeneous materials the response of a homogeneous (heterogeneous) materials is independent (dependent) of the position within the body.

Biological soft tissues are modeled using elastic materials model. The elasticity is the property of a solid material to return to its original size and shape when the influence of a external force is removed. In this case the strains are said to be reversible.

Considering small deformations, the stress-strain law of a linear material is given by the **Hook's law**

$$\sigma = \lambda \epsilon,$$

where the coefficient of proportionality λ is named **Young's modulus**.

For large deformation the stress-strain relationship is deduced from a potential function. A **hyperelastic** material is an elastic material for which the work is independent of the deformation path. The material reversibility and path-independent behavior implies the absence of energy dissipation during the deformation. Thus there exist a **potential** function $W(\epsilon)$ such that

$$S = \frac{\partial W(E)}{\partial E} = 2 \frac{\partial \psi(C)}{\partial C}$$

Moreover, if the material is isotropic, the stored strain energy W of a hyperelastic material can by written as a function of principal invariants (I_1, I_2, I_3) of the Green deformation tensor C previously defined in equation 3.9. Next, we introduce the most used potential functions for characterization of biological soft materials.

For the simplification of potential expressions we define the first and the second deviatoric strain invariant :

$$\bar{I}_1 = \frac{I_1}{I_3^{1/3}}; \quad \bar{I}_2 = \frac{I_2}{I_3^{2/3}}$$

We also define the *bulk modulus* as measure of a material's resistance to compression; the shear modulus as the ration of shear stress to the shear strain; and the Poisson ratio as the ration between longitudinal strain to the transverse strain describing the body shape change . For small deformation the bulk modulus and shear modulus are linked to the Young's modulus and Poisson ration by the next relations:

$$K = \frac{E}{3(1-2\nu)} \text{ and } \mu = \frac{E}{2(1+\nu)}$$

⁷⁰⁵ **Neo-Hookean potential function**

The Neo-Hookean law is an extension of the Hook's law to large deformations. The potential function is based only on the first invariant and is given by

$$W = \frac{\mu}{2}(\bar{I}_1 - 3) + \frac{K}{2}(J - 1)^2 \quad (3.25)$$

Where μ and K are initial shear modulus and initial bulk modulus respectively.

Mooney-Rivling potential function

⁷¹⁰ The potential function of a Mooney-Rivling material is defined as:

$$W = \frac{\mu_1}{2}(\bar{I}_1 - 3) + \frac{\mu_2}{2}(\bar{I}_2 - 3) + \frac{K}{2}(J - 2)^2 \quad (3.26)$$

Where the constants μ_1 and μ_2 describing the material properties are linked to the initial shear modulus $\mu = (\mu_1 + \mu_2)$. And the constant K is the initial bulk modulus.

Gent potential function

The potential function of a Gent material model is defined as:

$$W = -\frac{\mu J_m}{2} \ln \left(1 - \frac{\bar{I}_1 - 3}{J_m} \right) + \frac{K}{2} \left(\frac{J^2 - 1}{2} - \ln J \right) \quad (3.27)$$

⁷¹⁵ Where, as previous the μ and K constants are the initial shear modulus and the initial bulk modulus respectively. And J_m is the limiting value of $(\bar{I}_1 - 3)$

Governing equations of Lagrangian formulation

We consider a body β which occupies in the reference configuration the domain Ω_0 with a boundary Γ_0 . The governing equations for the mechanical behavior of a continuous body

⁷²⁰ are:

1. Conservation of mass $\rho_1 J = \rho_0$
2. Conservation of linear momentum $\nabla \cdot P + \rho b = 0$
3. Conservation of angular momentum $F \cdot P = P^T \cdot F^T$
4. Constitutive equations
5. Measure of strain $E = \frac{1}{2}(C - I)$
6. Boundary condition: $e_i \cdot N \cdot P = e_i \cdot \bar{t}$ on $\Gamma_0^{t_i}$
7. Internal continuity condition: $\llbracket e_i \cdot N \cdot P \rrbracket = 0$ on Γ_0^{int}

Where we note $\Gamma_0^{t_i}$ the set of prescribed traction \bar{t} on the body boundary Γ_0 ; and Γ_0^{int} is the union of all surfaces where the stresses are discontinuous in the body (material interfaces).
730

The momentum equation together with the traction boundary condition and interior traction continuity condition are called Generalized Momentum Balance (GBM).

3.3 Finite Element Discretization

As previously described, in continuous mechanics the body deformation is expressed in terms of partial differential equations (PDE). For the majority of problems, the PDEs cannot be solved analytically, therefore approximation methods are developed. To this end, the finite element (FE) method has become the standard numerical calculation to compute such approximations. The computational domain, the unknown solution, and its partial derivatives are discretized, so as to obtain a set of algebraic equations for the function values at a finite number of discrete locations. The unknowns of the discrete problem are associated with a computational mesh which represents a subdivision of the domain Ω_0 into many small control volumes Ω_k .
735
740

3.3.1 Eulerian and Lagrangian mesh description

The mesh description depends on the chosen independent variables (Eulerian or Lagrangian formulation). In a Eulerian mesh, the Eulerian coordinates of nodes are fixed (coincident with spatial points) and the material point change in time (see Figure 3.5.b). In this case the mesh has to be large enough to contain the body in its current configuration. Throughout the deformation the material points will belong to different elements. Whereas, in a Lagrangian mesh, the Lagrangian coordinates of nodes are time invariant, nodal trajectory corresponds with material points trajectory and no material passes between elements (see Figure 3.5.a).
745
750

In a Lagrangian mesh the boundary and interface nodes remains coincident with body boundaries and material interfaces throughout the entire deformation. Thus, the boundary conditions are defined directly on the respective nodes. On the other hand, in a Eulerian mesh the boundary and interface conditions have to be defined on point which are not nodes. This implies important complications in multi-dimensional problems.
755

An important drawback of a Lagrangian mesh affect mainly the large deformation domain. As the nodes are coincident with the material points, the elements deform with materials. Therefore, the magnitude of deformation is limited because of element distortion. The limited distortion that most elements can sustain without performance degradation or failure is a important factor in nonlinear analysis with Lagrangian formulation.
760

In conclusion, an Eulerian mesh formulation is usually used to solve problems linked to fluid like materials and a Lagrangian mesh for solid like materials.

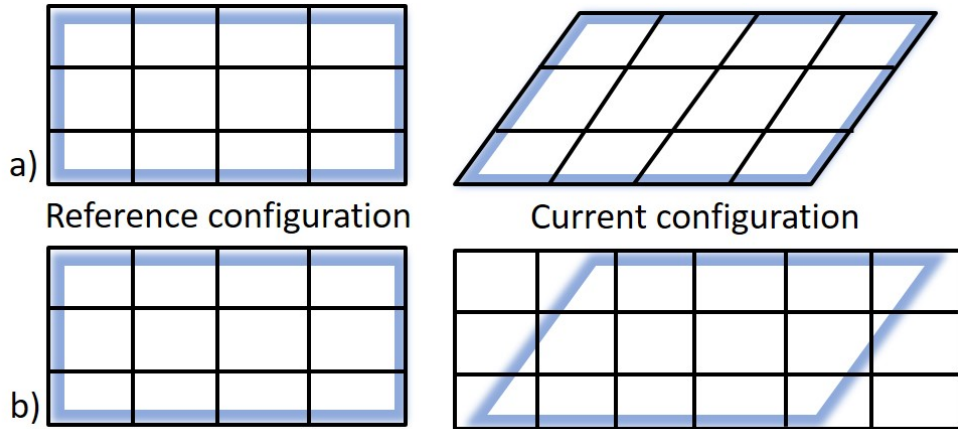


Figure 3.5: a) Lagrangian mesh formulation. b) Euler mesh formulation

3.3.2 Lagrangian mesh

765 subsection:lagrangianmesh

The general approach of the FE method in Lagrangian formulation is shown in Fig. 3.6. First the momentum equations with given boundary conditions is multiplied by an appropriate test functions. The test function has to satisfy all displacement boundary conditions and to be smooth enough so that all derivatives in momentum equations are well defined. Then performing an integration by parts, the week formulation of GMB is obtained, also called the principle of virtual work. cite Belytschko

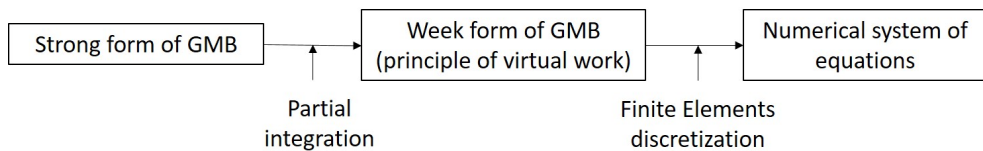


Figure 3.6: From strong formulation of the generalized momentum balance to numerical equations.

The momentum equations and the traction boundary conditions, usually called the strong form, cannot be directly discretized by FE method. The strong formulation of the GBN equations impose the C_1 continuity conditions on the field variables. Therefore, 775 the solution of this problem does not always exist. This is true especially in the case of complex domains with different material interfaces. In order to overcome these difficulties, weak formulations are preferred. The week formulation of GMB reduce the continuity requirements thereby allowing the use of easy-to-construct and implement polynomials. Because of the reduction in the requirements of function smoothness, the weak forms 780 never give an exact solution but one can obtain a relatively accurate solution with the discretization refinement.

From the weak form of the GBM equations, the numerical system of equations is formulated by using finite elements interpolants for the mechanical displacement and the test functions. The whole domain is discretization into a number of smaller areas or volumes which are called **finite elements** and their assembly is called a **mesh**. Elements can be of various shapes (as shown in Figure 3.7.a), quadrilateral or triangular in two dimensions, and tetrahedral or hexahedron in three-dimensions.

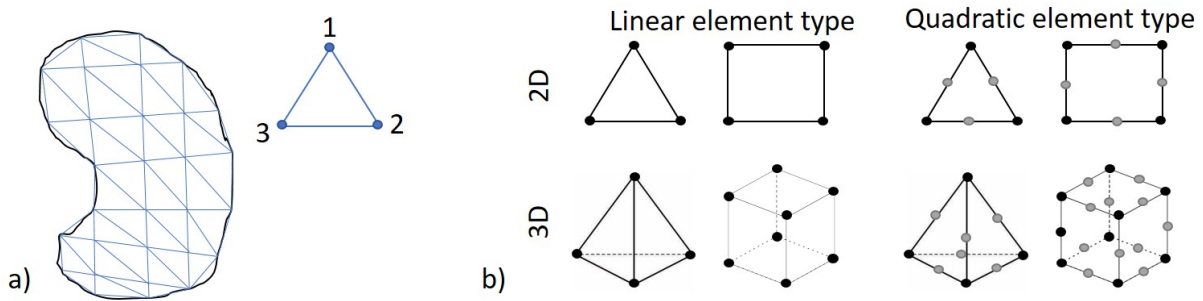


Figure 3.7: a) Discretization of a 2D domain with triangular finite elements :Lagrangian mesh . b) Different types of finite elements

The mechanical displacement is approximated at the discretization points called finite element **nodes**. The nodes are at the corners of the elements for a linear type, and at the corners and midsides of the elements for a quadratic type (figure 3.7.b). The displacement of each point within an element is fixed by the values of the displacements of the nodes of the element. In this way, the problem of finding the displacement of every point within the body is replaced by the problem of finding the displacements of a finite number of points.

As in a Lagrangian mesh the nodes are following the motions, for large deformation the finite elements can be highly distorted. Therefore, the shape quality is generally followed all along the deformation process. Several shape parameters as a function elements geometry have been proposed as: aspect ratio, maximum corner angle, Jacobian ratio, skewness, parallel deviation, warping factor. The acceptable limit values are proper to the elements types.

In the following only shape parameters of linear triangular elements are presented.

Triangle aspect ratio

The element's shape aspect ratio is computed using only the corner nodes of the element (Figure 3.8). First, two lines are created: one through a node (K) and the midpoint of the opposite edge (K'), the second through the midpoint of the others two edges (J' and I'). Then two rectangles are created, each rectangle have a pair of edges parallel to one of previously defined lines. The rectangle edges have to pass through the nodes and the triangle's edges midpoints. This construction is repeated for each triangle's node resulting in 6 rectangles. The aspect ratio of a rectangle is defined as the ration between the longer

and shorter side. Thus, the triangle's aspect ratio is defined as the maximal aspect ratio over the 6 rectangles divided by squared root of 3.

The best possible aspect ratio is 1 and is represented by an equilateral triangle. An element with an aspect ratio larger than 20 is considered as bad aspect element, large aspect ratio may degrade solution performance.

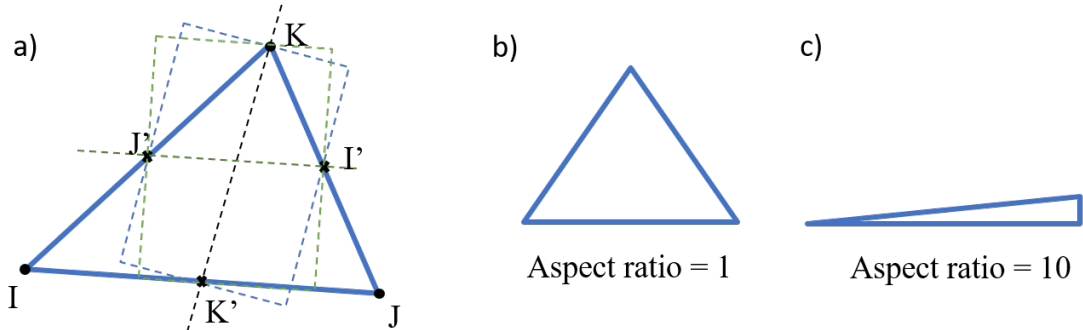


Figure 3.8: Computation of aspect ratio for a triangle

Triangle maximum corner angle

The maximum corner angle is computed using nodes position in 3D space. The best possible maximum corner angle is 60° . An element having a maximal corner angle larger than 165° is considered as bad shape element, large corner angles may degrade the solution performance. Figure 3.9 shows a triangle with a good (60°) and bad (165°) quality.

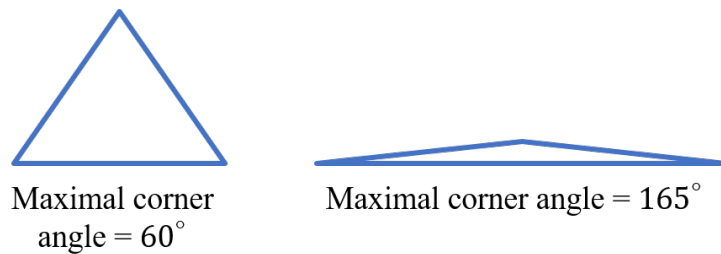


Figure 3.9: Example of triangles with different maximal corner angles.

The aspect ratio and the maximal corner deviation of a tetrahedra is computed using the definition of the same measure on a triangle. The elements shape parameter is assigned as the worst value over the triangles defined by the tetrahedra's faces and cross-sections.

Skewness

The skewness of a triangular element is computed using the equivalent volume deviation method. It is defined as the difference between the optimal and real cell size over the

825 optimal cell size. The optimal size is the size of an equilateral cell with the same circumradius. According to its definition, the value of 0 indicates an ideal cell, from 0 to 0.75 the cell is considered to have a good quality, from 0.75 to 1 the cell is considered to have a bad quality and a value of 1 indicates a completely degenerated cell (Figure 3.10).

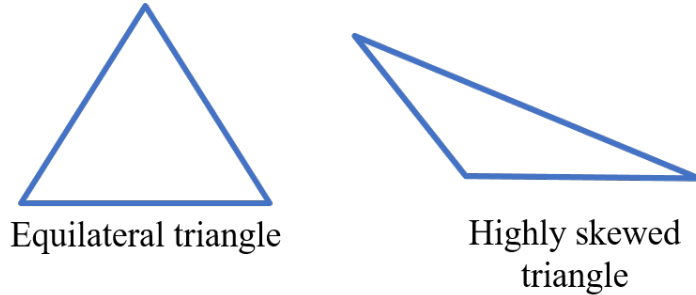


Figure 3.10: Example of triangles with different skewness.

3.4 Contact mechanics

830 In order to transfer the loads between elements, the nodes have to be connected together. If two bodies are separated with no commune nodes, no interaction will occur during the deformation and the bodies will pass through each other. Here, an asymmetric surface-to-surface contact method is used to solve the multi-body interaction problems.

Let's consider two different bodies \mathcal{A} and \mathcal{B} and their occupied domains Ω_A and Ω_B with boundaries Γ_A and Γ_B respectively (see Figure 3.11). Also, we note Ω the domain of intersection of two bodies. The contact interface is the intersection of the surfaces of the two bodies:

$$\Gamma = \Gamma_A \cap \Gamma_B.$$

The intersection consists of two surfaces distinguished as **target** and **contact** surfaces.
835 The choice of the surfaces is made following the next guidelines:

- if the one body \mathcal{A} is stiffer than the body \mathcal{B} , the surfaces Γ_A define the target and Γ_B the contact surface;
- if Γ_A is a concave surface getting in contact with the convex surface Γ_B , the surface Γ_A define the target and Γ_B the contact surface.
- if the surface Γ_A is larger than Γ_B , the surface Γ_A denote the target and the Γ_B the contact surfaces.

840 For the following, we identify Γ_A as the target surface and Γ_B as the contact surface (Figure 3.11).

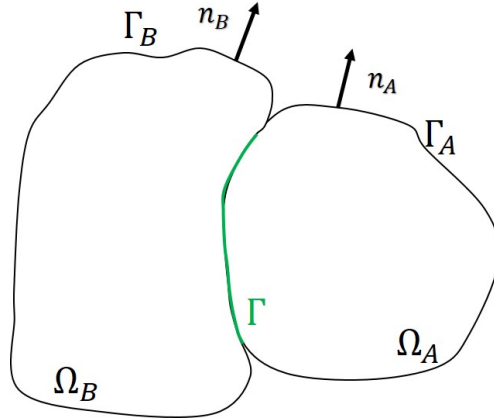


Figure 3.11: Multi-body contact problem.

3.4.1 Contact interface equations

- ⁸⁴⁵ In a multi-body interaction process, in addition to standard governing equations, two more contact conditions have to be fulfilled: the two bodies cannot interpenetrate and the traction must satisfy momentum conservation on the contact interfaces.

Traction conditions

- ⁸⁵⁰ Traction conditions must follow the balance of momentum across the contact interface:

$$t_A + t_B = 0 \quad (3.28)$$

On the contact boundary surface Γ the traction vectors are decomposed into its normal and tangential components:

$$\begin{aligned} t_A^n &= t_A \cdot n_A, & t_B^n &= t_B \cdot n_B \\ t_A^t &= t_A - t_A^n n_A, & t_B^t &= t_B - t_B^n n_B \end{aligned}$$

Therefore the momentum balance requires:

$$t_A^n + t_B^n = 0, \quad t_A^t + t_B^t = 0 \quad (3.29)$$

Inter-penetrability condition

- ⁸⁵⁵ The bodies implied in a multi-body problem must fulfill the inter-penetrability condition:

$$\Omega_A \cup \Omega_B = \emptyset \quad (3.30)$$

Decomposing the displacement u into normal and tangential components u^n and u^t respectively the inter-penetrability condition can be written as:

$$t^n \leq 0, \quad u_n - g \leq 0, \quad t_n(u^n - g) = 0 \quad (3.31)$$

Where g is the gap between the two bodies.

3.4.2 Surface interaction models

When two solid bodies are placed together under a nonzero normal force and acted upon by another tangential force, a **friction force** $f_{friction}$ tangential to the interface and opposite to the applied force is created. Depending on whether the applied force can overcome the friction force opposing it, the bodies may or may not move relative to the other. The body motion along the interface is called **sliding**. The **sliding force**, $f_{sliding}$ is the applied tangential force which cause the sliding motion between the two bodies.

The problem in determining whether relative motion will or will not occur is one of balancing the involved forces. According to allowed relative body motion in tangential or normal directions, five types of surface interaction models are distinguished: bonded, rough, no-separation, frictional and frictionless. Table 3.1 resume each mechanical behavior. If the body motion is not allowed in normal or tangential direction, once the bodies get in contact, the respective components of traction are equals $t_A = t_B$. Which means that, for a pure **bonded** contact, the two bodies are considered as a unique solid body.

Name	body motion in normal direction	body motion in tangential direction
Bonded	No	No
Rough	Yes	No, $f_{friction} \gg f_{sliding}$
No-separation	No	Yes, $f_{friction} = 0$
Frictionless	Yes	Yes, $f_{friction} = 0$
Frictional	Yes	Yes, if $f_{sliding} > f_{friction}$

Table 3.1: Surface interaction models and behaviors

Frictional contact behavior is defined using Coulomb friction law. For a continuous body the Coulomb friction model is applied at each point of the contact interface. Consider that bodies \mathcal{A} and \mathcal{B} which are in contact within the surface Γ , then for all $x \in \Gamma$:

$$\text{if } \|t^t(x)\| < -\mu_f t^n(x), \quad \Delta u^t = 0 \quad (3.32)$$

$$\text{if } \|t^t(x)\| = -\mu_f t^n(x), \quad \Delta u^t = -k(x)t^t(x), \quad k(x) > 0 \quad (3.33)$$

Where μ_f is the material property named **friction coefficient**, Δu^t is the slip incremental in the tangential direction and $k(x)$ is a variable computed from the momentum equation. The condition 3.32 is known as sticking condition: the tangential traction is less

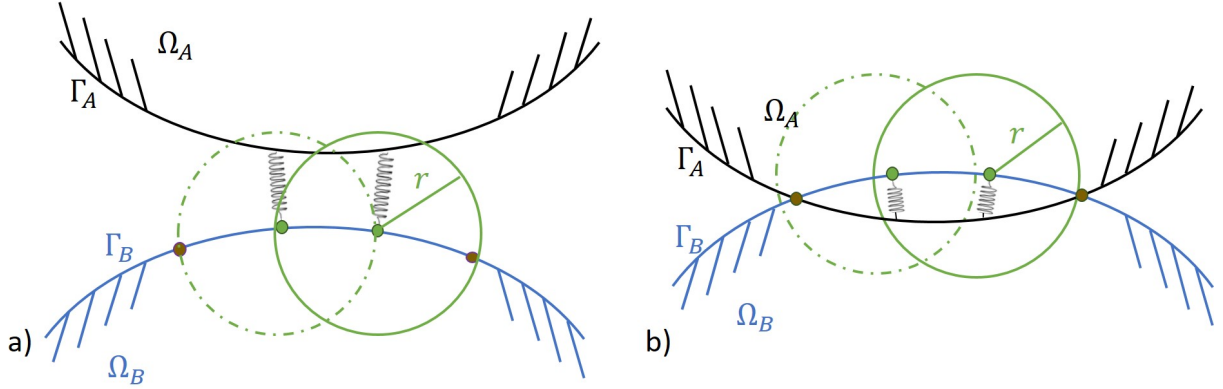


Figure 3.12: Contact status update using a pinball of radius r .

than the critical value, thus no sliding occurs. Reciprocally, condition 3.33 is called sliding condition.

Then a frictionless contact model is used, $\mu_f = 0$, the tangential tractions vanish completely: $t_A^t = t_B^t = 0$. Then rough contact is modeled the friction coefficient μ_f is equal to infinity, therefore sticking condition is always fulfilled.

Several contact models can be combined to model a physical contact between two bodies.

3.4.3 Contact formulation algorithm: Pure Penalty model

Pinball region

Contact problem present two primary difficulties. First is the traction conditions computation when frictional models are considered. And second is the unpredictability of regions which will get in contact with each other during the deformation process.

The region of contact depends on materials properties and imposed boundary conditions; therefore, it is very difficult to know a priori where the surfaces will come in contact. To formulate analytic equations, one has to know exactly the nodes involved in the contact process. Therefore, during the body deformation the program calculates if the contact is opened or closed. The status is defined using a sliding pinball (Figure 3.12). The pinball slide over the contact surface points and search for the target surface. If the node to surface distance is smaller than the pinball radius the contact is considered closed otherwise the contact is considered opened.

900

Distance measures

Let's consider a point x_B belonging to the body surface Γ_B and x_A the intersection point of the surface normal n_B with the surface Γ_A (Figure 3.13). The point to surface distance

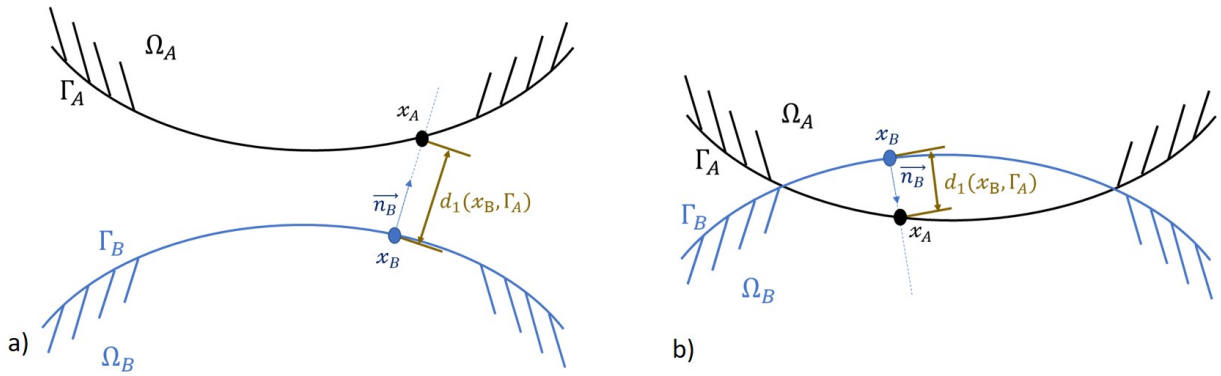


Figure 3.13: a) Body \mathcal{A} and body \mathcal{B} are close but not in contact. The $d_1(x_B, \mathcal{A})$ measure define the gap between the bodies at point x_B . b) Body \mathcal{B} have penetrated the body \mathcal{A} . The $d_1(x_B, \mathcal{A})$ measure gives the penetration at point x_B .

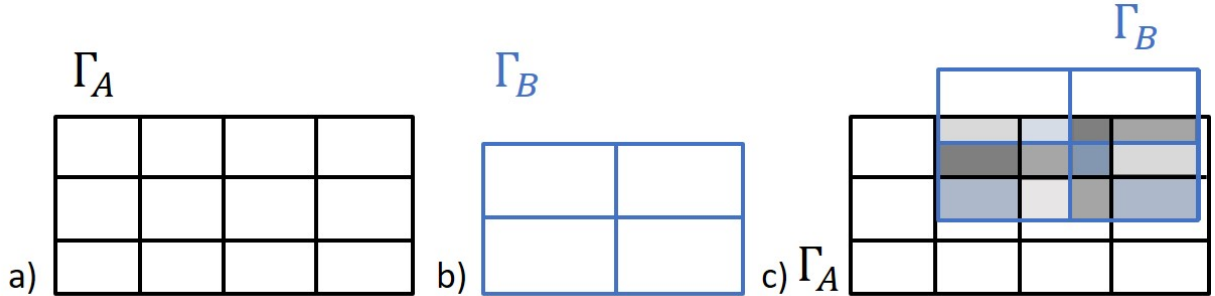


Figure 3.14: The contact surface projection over the target surface: a) Target discretized area; b) contact discretized area; c) intersection of the projected surfaces.

$d_1(x_B, \mathcal{A})$ is defined as:

$$d_1(x_B, \mathcal{A}) = \|x_B - x_A\| = \left[\sum_{i=1,2,3} (x_B^i - x_A^i)^2 \right]^{\frac{1}{2}} \quad (3.34)$$

905

If the intersection point x_A is located inside the pinball area, the node to surface distance define the amount of **gap** or **penetration** at the respective point (Figure 3.13).

Computing the gap or penetration at single points increase numerical instabilities. Therefore, in this work, the gap and penetration are computed in an averaged manner over 910 the projected surface areas. Figure 3.14 show the projected surface areas (c) obtained by the intersection of the target surface (a) with the projected contact surface (b).

The interested reader is referred to ANSYS contact technology guide for more details on the contact modeling.

915 **Finite element mesh**

For the finite element calculus, contact and target surfaces have to be discretized in 2D linear or quadratic elements consistent with the underling 3D element mesh (Figure 3.7). The elements are named contact and target elements respectively. They have no material properties apart the friction coefficient μ_f . The stress-strain as well as the gap or penetration
920 measures are computed for each mesh node of the discretized surface.

Pure Penalty method

In this work, mathematical expression of contact compatibility conditions is formulated using penalty method. Then one is using penalty contact formulation, additional contact properties are defined to manage contact behavior as: normal stiffness factor, tangential
925 stiffness factor and contact opening factor. The latter constants play an important role in the numerical calculus but have no physical meaning.

The penalty method uses a spring like relationship to introduce a force for all nodes pairs (contact-target) that are defined to be in closed contact (Figure 3.34). The contact force is computed using the following expression:

$$f_c = k_c d \quad (3.35)$$

930 where d represents the penetration or gap amount and k_c is the normal contact stiffness of opening contact stiffness constants respectively. The tangential contact stiffness works in the same way enforcing the responding frictional force. Some finite amount of penetration, $d > 0$, is required mathematically to maintain equilibrium. However, physical contacting bodies do not interpenetrate ($d = 0$).

935 The biggest challenge here is that the magnitude of the stiffness contact constants is completely unknown beforehand. The contact force at each node have to be large enough to push the contact surface back to the target surface and eliminate unwanted penetration or gap. In the same time, if the contact force is too large, it pushes the contact surface far away from the pinball region causing error and solution instabilities.

940 **3.5 Breast biomechanical model: overview**

Biomechanical modelling of breast tissues is widely investigated for various medical applications such as surgical procedure training, pre-operative planning, diagnosis and clinical
945 biopsy, image guided surgery, image registration, and material parameter estimation (Table 3.3). For the last 20 years, several research groups have presented their breast models based on finite elements theory. The complexity and relevance to breast anatomy of each model depend on the research purpose for which it was designed.

As described in Section 3.2, to build a mechanical breast model, one need to provide the breast geometry in a **reference configuration**, the **constitutive models** of tissues composing the breast volume and the **boundary conditions**. The definition of all variables
950 has an significant impact on model accuracy.

3.5.1 Breast reference configuration

A large number of existing patient specific models are using volumetric data from MR images Carter (2009b), Kellner et al. (2007), Conley et al. (2015) Eiben et al. (2016b), Martínez-Martínez et al. (2017) or CT images Palomar et al. (2008), Sturgeon et al. (2016)
955 to compute the breast geometry. Acquired data represents deformed breast soft tissues due to in-vivo conditions, and therefore initial pre-stresses are included. Generally, for breast deformation simulations, the reference configuration is chosen to be the breast geometry in a stress-free configuration, without being deformed by any force, including gravity.

The initial pre-stresses are generally unknown and it is extremely difficult to measure
960 them in clinical conditions. The bibliography presents four different strategies allowing to estimate the breast reference configuration.

Prone breast configuration

Considering existing image modalities, in a clinical framework woman breast is compressed only in a up-right or prone body position. Therefore, Han et al. (2012), Ruiter et al.
965 (2006) and Sturgeon et al. (2016) have estimated breast compression starting from breast configuration in prone body position, neglecting tissues pre-stresses. This assumption is justified only for a breast compression simulation, as the gravity induced pre-stresses are negligible when compared to the compression induced stress. However, for a different framework, as a multi-loading simulation the latter assumption highly penalizes simulation
970 results.

Inverse gravity

(Palomar et al., 2008; Sturgeon et al., 2016) used the inverse gravity method to estimate the stress-free geometry. In their work, the authors just reversed the gravity effects without consideration of pre-stresses of breast tissues in prone configuration. According to Eiben
975 et al. (2014) the inverse gravity methods gives a poor approximation of the breast reference state and can be used only with small deformations or highly constrained models.

Breast neutral buoyancy configuration

Assuming that breast density is equal to water density, Rajagopal et al. (2008) compute the breast stress-free configuration by imaging the breast immersed in water. Following the
980 same physical assumptions, Kuhlmann et al. (2013) proposed to estimate the stress-free configuration by applying a hydro-static distributed load on the breast surface in prone configuration. Even though the estimated geometries are accurate enough, these methods are time-consuming and in very uncomfortable in a clinical framework.

Prediction-correction iterative algorithm

985 The prediction-correction method was first proposed by (Govindjee and Mihalic, 1998) and adapted later by Carter (2009b) and Eiben et al. (2014). The original method is based on the prediction-correction iterative scheme represented in Figure 3.15. The first approximation of the breast reference configuration is estimated by applying the inverse gravity method on prone breast configuration (see section 3.5.1). Next, a numerical breast
 990 prone configuration is computed and compared to the corresponding measured one. The difference between the two geometries used to update the reference breast configuration. The process is repeated until the convergence is achieved. The methods were validated using the neutral buoyancy breast shape.

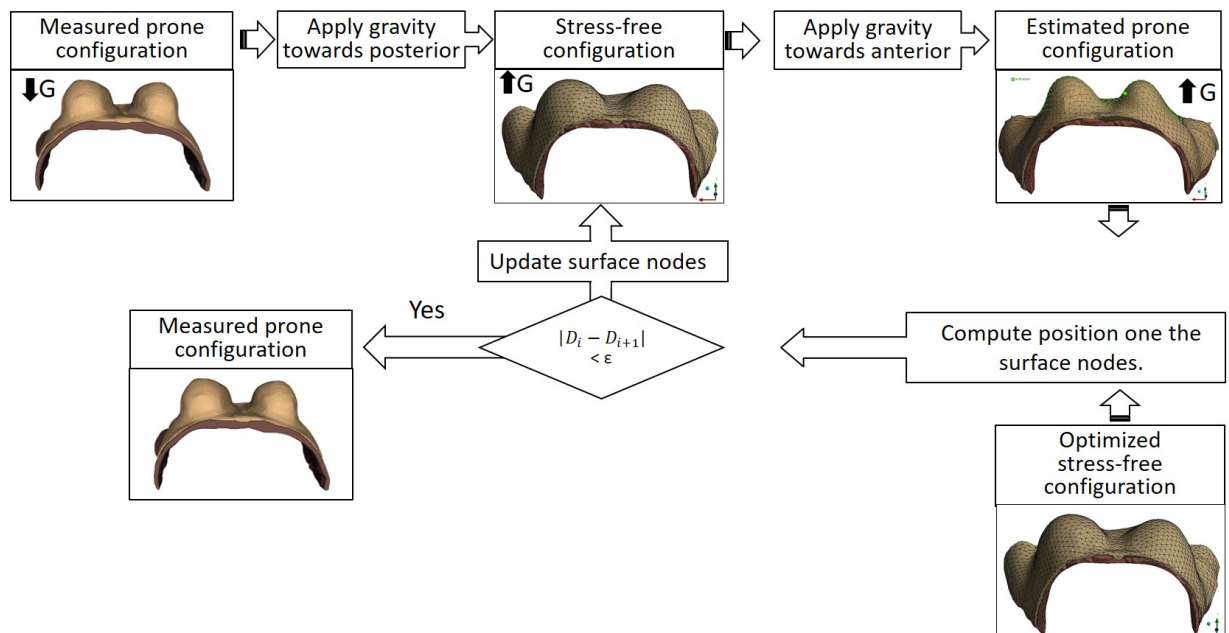


Figure 3.15: Prediction-correction algorithm

Inverse FE algorithm

995 Pathmanathan et al. (2008) and later Vavourakis et al. (2016) proposed an analytic computation of the reference state of breast by reparametrizing the equilibrium equation and solving finite elements formulation of the inverse motion. The model provides good estimates of breast reference configurations but need large numerical resources. Eiben et al.
 1000 (2014) showed that, the prediction-correction iterative algorithm and the inverse FE algorithm are similar in terms of resulting accuracy.

3.5.2 Constitutive models

Global breast mechanics are governed by breast tissue compositions and their individual mechanical properties. The breast soft tissues are known to be incompressibles, nonlinear, anisotropic, and viscous materials. However, according to Wellman et al. (1999) the breast tissues viscosity can be neglected when the mechanical load is applied within short time scales.

Under large compression and body position change the breast volume varies due to the blood flows, thus soft tissues are frequently modeled as quasi-incompressible materials with a Poisson ratio ranging between $\nu = 0.45 - 0.5$. The influence of the Poisson ratio within linear constitutive models was studied by Tanner et al. (2006), according to the authors the best estimates are obtained with high Poisson ratio ($\nu = 0.495, 0.499$). The soft breast tissues are predominately composed of water; therefore, the density is considered to be equal to 9810 kg/m^3 .

For the last decades several constitutive models were used to model the breast tissues response to a external force: exponential elastic (Azar et al., 2002), Neo-Hookean hyperelastic (Carter, 2009b; Rajagopal et al., 2010; Sturgeon et al., 2016; Eiben et al., 2016a; Han et al., 2014; Garcia et al., 2017), Money-Rivling (Samani et al., 2007; Tanner et al., 2006; Carter et al., 2012; Martínez-Martínez et al., 2017). Eder et al. (2014) compared the most popular models in a multi-loading gravity simulation, according to the authors the Neo-Hookean model proposed by Rajagopal et al. (2008) gives the best estimates.

Glandular and adipose tissues biomechanical properties

Multiple studies have shown that breast composition and so its mechanical behavior undergo substantial changes during woman lifetime (section ??). The first studies on mechanical proprieties estimation of breast tissues were done in diagnostic purposes. Then the breast is developing benign or malign disorders, their mechanical properties differ from the ones of the normal breast tissues. In a study of 142 simples, bellowing to 4 type of tissues, Krouskop et al. (1998) found that depending on the pre-compression level Youngs modulus of invasive carcinoma is from 5 to 25 times larger than the one of normal adipose tissue (from 5% to 20% pre-compression).

Later, several research groups (Table 3.2) have studied the elastic modulus of adipose and glandular tissues. The breast tissues elastic parameters range between 0.1 kPa and 271.8 kPa. Such big variation may be explained by the differences in the used experimental set-up but also by the participant's physical condition, age or period of the menstrual cycle. For example, Han et al. (2012) though using the same FE method, found significantly inter-individual variability, with the shear modulus ranging between $0.22 - 43.64 \text{ kPa}$. Lorenzen et al. (2003) showed that during the menstrual cycle, due to the hormonal changes, the elastic properties of the glandular tissues can change by about 30%.

An important difference in estimated values of elastic modulus of breast soft tissues is observed between the linear elastic and hyperelastic models. If only in-vivo studies with Neo-Hookean material models are considered, the range of the adipose and glandular shear

Ex-vivo estimation				
Author	Method	Material model	material properties	
			Adipose kPa	Glandular kPa
Krouskop et al. (1998)	Indentation-5%	Linear elastic	$E = 19 \pm 7$	$E = 33 \pm 11$
Krouskop et al. (1998)	Indentation-20%	Linear elastic	$E = 20 \pm 6$	$E = 57 \pm 19$
Wellman et al. (1999)	Indentation - 5%	Linear elastic	$E = 6.6$	$E = 33$
Wellman et al. (1999)	Indentation - 15%	Linear elastic	$E = 17.4$	$E = 271.8$
Samani and Plewes (2004)	Indentation	Linear elastic	$E = 3.25 \pm 0.91$	$E = 3.24 \pm 0.61$
In-vivo estimation				
Van Houten et al. (2003)	MRE	Linear elastic	$E = 17 - 26$	$E = 26 - 30$
Sinkus et al. (2005)	MRE	Visco-elastic	$\mu = 2.9 \pm 0.3$	
Rajagopal et al. (2008)	MRI-FEM	Neo-Hookean	$\mu = 0.16$	$\mu = 0.26$
Carter (2009a)	MRI-FEM	Neo-Hookean	$\mu = 0.25$	$\mu = 0.4$
Han et al. (2012)	MRI-FEM	Neo-Hookean	$E = 1$	$E = 0.22 - 43.64$
Gamage et al. (2012)	MRI-FEM	Neo-Hookean	$\mu = 0.1$	
Griesenauer et al. (2017)	MRI-FEM	Hooke's law	$E = 0.25$	$E = 2$

Table 3.2: Material properties for adipose and glandular tissues.

modulus is significantly lower than $50 kPa$.

Carter (2009b) compared one parameter Neo-Hookean potential function with five parameters Money-Rivling potential function for various material properties. The multy-loading gravity simulation were thus performed on 3 subjects. According to the authors 1045 the Money-Rivling models underestimates the tissues deformation by at least 75% then the subject is re-positioned from the supine to the prone positions. The best estimates were given by the Neo-Hookean model with the initial shear modulus equal to $0.2 kPa$.

Previously listed researches clearly showed the variability of elastic modulus of the same tissue between and within individuals. Eder et al. (2014) made a larger analysis including

1050 all material models proposed in the literature. According to authors, many of them are too stiff permitting not enough deformation within the gravity loading. The most reliable identified values is the ones given by Rajagopal et al. (2008) (Table 3.2).

Muscle biomechanical properties.

Skin biomechanical properties

1055 Several studies shown the importance of skin in biomechanical breast modeling. According to Carter (2009b), a model which include the skin estimate better the tissues deformation under gravity loading.

1060 Sutradhar and Miller (2013) published a complete study of breast skin estimating its elasticity for 16 different breast regions. The study was done on 23 female volunteers aging from 29 to 75 ears. The authors found that the skin elastic modulus range between 15 – 480kPa with an average of $334 \pm 88\text{kPa}$. The elastic modulus in the lateral region (mean 370kPa) has the highest value followed by the superior region (mean 355kPa). The inferior region (mean 331kPa) follows next, with the medial region having the lowest value (mean 316kPa). However, no significant variation of elastic modulus in radial direction was found.

1065 Other researches on skin elasticity are available, but they are not specific to the breast skin. Hendriks et al. (2006) estimated in-vivo skin proprieties by suction testing. The skin was considered as a homogeneous, isotropic, incompressible, hyperelastic material. The study was performed on 14 subjects and the obtained average of elastic modulus for skin was 58.4kPa .

1070 The estimation of the breast skin elasticity by the means of finite elements using Neo-Hookean potential function has resulted in softer materials model. Carter (2009a) found a initial shear modulus equal to 16kPa , whereas Han et al. (2014) found that for the five studied subjects the skin shear modulus ranged between 2.47kPa and 5.78kPa .

1075 Fascias and ligaments biomechanical properties

The surrounding breast fascias and the supervisory ligament form the breast support matrix. These structures are wall described for surgical purposes (thickness, location etc), however little is known about their mechanical properties. The first biomechanical breast model taking into account the effect of Cooper's ligaments was proposed by Azar et al. 1080 (2002) and took up later by Pathmanathan et al. (2008) and Han et al. (2012). The authors designed a new material model for fatty tissues including the anisotropic behavior of breast ligaments. Later, Georgii et al. (2016) come up with a spring-mass generic model for the breast support matrix. According to the authors, including the ligaments into the finite elements breast model have increased the robustness of the prone-supine simulation 1085 with respect to the input parameters.

To our knowledge, where are no experimental data describing the mechanical properties of breast superficial fascia. An approximation of the elastic modulus of Cooper's ligaments is given by Gefen and Dilmoney (2007) by extrapolating from known ligamentous structure

in the human body. The authors estimated the elastic modulus of suspensory ligaments to
1090 relay between $80 - 400 \text{ MPa}$

The fibrous tissues obtain their elasticity from elastic fibers and their structural support from collagen fibers. As reported by Riggio et al. (2000) the superficial fascia is made up of both collagen and elastic fibers. In contrast, the Cooper's ligaments appeared to be composed almost of collagen fibers. The mechanical properties of a single collagen fiber
1095 from a rat tail were studied by Wenger et al. (2007), according to authors their elastic modulus range between 5 GPa and 11 GPa . Other studies on biomechanical characterization of human body superficial fascia are available in literature. The most frequently studied is on the plantar fascia and foot ligaments with a Young's modulus ranging between 0 MPa and 700 MPa (Cheung et al., 2004; Kongsgaard et al., 2011).

1100 **3.5.3 Boundary conditions**

Direclet conditions are usually used to constrain the sternum/axilla ends and the posterior surface of the breast or the thoracic cage if the muscular tissues are considered (Griesenauer et al., 2017; Rajagopal et al., 2008; Pathmanathan et al., 2008; Gamage et al., 2012; Griesenauer et al., 2017). As reported by Carter (2009b) the zero-displacement boundary
1105 conditions in a multi-gravity loading framework result in a over-constrained model and sliding conditions on the mesh nodes corresponding to the chest wall have to be considered.

Later, several teams using biomechanical breast models for multy modality image registration or surgical planing showed what included the sliding boundary conditions (Georgii et al., 2016; Han et al., 2014) improve the registration accuracy. However those studies
1110 were the biomechanical model is designed for breast compression, the tissues sliding over the chest wall is neglected and fixed boundary conditions are usually assumed (Sturgeon et al., 2016; Martínez-Martínez et al., 2017).

3.5.4 Conclusion

During the last decades, several breast biomechanical models were proposed however, only
1115 a small part of them (Carter, 2009b; Gamage et al., 2012; Han et al., 2014) were evaluated with respect to the real tissues deformation. As we intend to build-up a subject specific breast biomechanical model capable of estimating multi-loading gravity deformations our assumption will rely only on already evaluated model within a same framework.

Today's outstanding breast biomechanical models are represented by the next three
1120 models: Eiben et al. (2016c), Han et al. (2014), Gamage et al. (2012). Gamage et al. (2012) proposed a finite elements model capable to estimate the supine breast configuration from the prone one. To assess the quality of fit, the root-mean-squared error (RMSE) form the point to surface distance was computed. Conform to the authors, the breast supine geometry was estimated within an RMSE of 5mm (maximal distance of 9.3 mm). In the
1125 same time, Han et al. (2014) developed a breast biomechanical model for image registration. The estimates were computed for five subjects, and the accuracy was assessed by computing the Euclidian Distance (ED) between anatomical landmarks. The mean ED range between

11.5 mm and 39.2 mm (maximal ED range between 20.3mm and 61.7mm). Finally, Eiben
et al. (2016c) proposed a new model to estimate the up-standing breast configuration from
₁₁₃₀ the prone one. The model was evaluated on 3 subject. The supine configuration was then
computed from the prone one and the quality of fit was measured in terms of the mean
Eulerian Distance between manually selected internal landmarks. Thus, the supine breast
configuration was estimated within a mean distance ranging between 12.2mm and 19.8mm.
The model evaluation for the up-standing configuration was not presented.

Authors	Application	FE mesh	Material models	Boundary conditions	Stress-free config.
Azar et al. (2002)	Computer assisted breast surgery	8-Node hexahedrons (trilinear isotropic elements)	Skin-elastic adipose,glandular-hyperelastic polynomial	Sliding between breast - thorax and breast-paddle	Prone breast geometry
Rajagopal et al. (2007)	Breast compression	8-Node hexahedrons (tricubic Hermite elements)	Homogeneous , Neo-Hookean model	Zero-displacement BC	Buoyant breast in water
Pathmanathan et al. (2008)	Image registration	8-Node hexahedrons (trilinear elements)	Homogeneous polynomial Skin exponential hyperelastic	Zero-displacement on muscle; Compression with imposed displacement	Inverse FE algorithm
Han et al. (2014)	Image registration	4-Node tetrahedrons	Muscle, glandular, fatty, skin - Neo-Hookean model	Sliding on pectoral muscle	Inverse gravity
Gamage et al. (2012)	Computer assisted breast surgery	8-Node hexahedrons (tricubic elements)	Homogeneous+ Neo-Hookean incompressible model	Zero-displacement BC on rib cage surface, Sternum, axilla ends, shoulder	PC iterative algorithm
Patete et al. (2013)	Computer assisted breast surgery	4-Node tetrahedrons (trilinear isotropic elements)	Adipose , glandular, skin	Zero-displacement BC on the chest wall	PC iterative algorithm
Kuhlmann et al. (2013)	image registration	4-Node tetrahedrons	Adipose, glandular-gel-like (Eulerian formulation); Skin - hyperelastic material (Lagrangian formulation)	Zero-displacement chest wall	PC iterative algorithm
Georgii et al. (2016)	Surgery simulation	8-Node hexahedrons, 2-node 3D spars	homogeneous elastic material, Cooper's ligaments-generic mass-spring model	sliding BC (breast on the pectoral muscle)	NA
Eiben et al. (2016c)	Surgery outcome prediction	4-Node tetrahedrons	Fatty , glandular-Hookean model; exponential hyperelastic	Zero-displacement BC	Inverse FE algorithm
(Garcia et al., 2017)	3D breast lesion localization	4-Node tetrahedrons	adipose, glandular - Neo-Hookean models	zero-displacement BC	Prone breast configuration

Table 3.3: Breast biomechanical models

A new biomechanical breast model

4.1 Introduction

- Explain that the image pre-processing was applied on both breast volumes.
 - Explain that the breast biomechanical model was built only on the second subject

¹¹⁴⁰ 4.2 Data acquisition and preprocessing

4.2.1 Data acquisition

To assess the entire breast volume as well as the surrounding soft tissues, the MR image modality is used. The images were acquired with a Siemens 3T scanner with T2 weighted image sequences. The in-plane image resolution was $0.5 \times 0.5 \text{ mm}$, and the slice thickness was 0.6 mm. During this acquisition, the contact between the breasts and the contours of the MRI tube, or with the patient body (arms, thorax), was minimized.

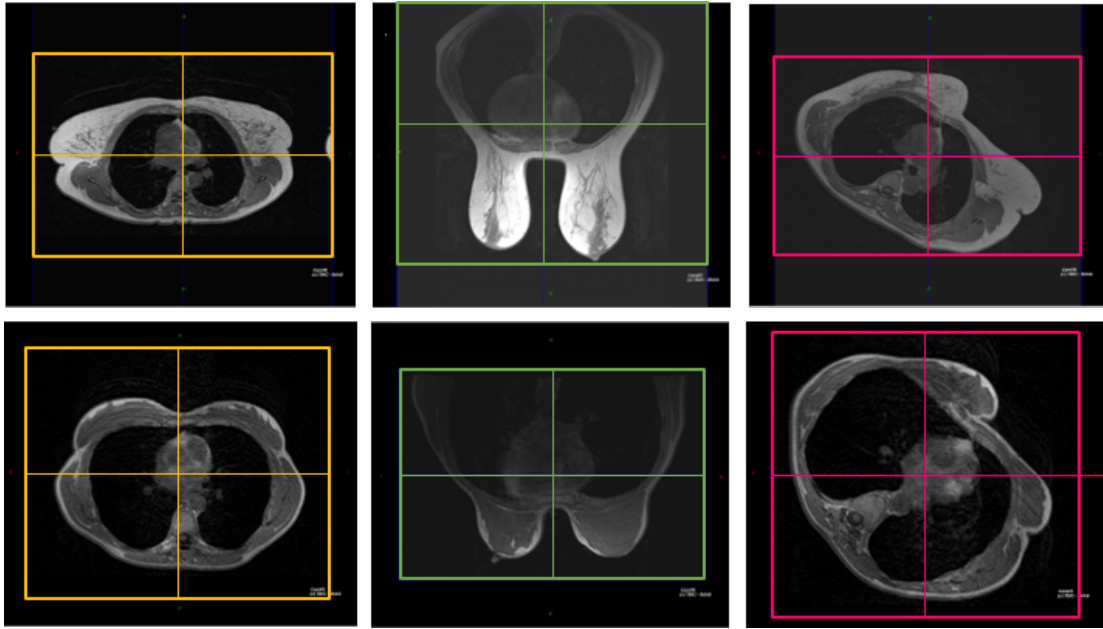


Figure 4.1: MRI images in three breast configuration: first line- subject 1; second line- subject 2

The two volunteers taking part to this study agreed to participate in an experiment part of a pilot study approved by an ethical committee (MammoBio MAP-VS pilot study). The volunteers are 59 and 58 years old and have A-cup (subject 1) and F-cup (subject 2) breast size respectively.

Three different positioning configurations are considered: prone, supine and supine titled (45 deg). The positions were chosen to assess the largest possible deformations with minimal contact areas between the volunteer and the relatively narrow MRI scanner tunnel.

The volunteers were also asked to provide the compression force and breast thickness as measured on their most recent mammograms. Such data are summarized in Table 4.1.

	Subject 1		Subject 2	
	Right breast	Left breast	Right breast	Left breast
Force (N)	21.9	40.9	94.8	56.6
Breast thickness (mm)	47	42	50	49

Table 4.1: Compression force and breast thickness for both subjects for a cranio-caudal mammogram

4.2.2 Image segmentation

A semi-automated active contour method proposed by ITK-Snap software is used to segment the pectoral muscle, the breast and the internal organs from MR images.

The segmentation process for one tissue type is performed progressively by small regions of interest (ROI, see Figure 4.2.a). For each ROI the segmentation of one tissue takes place in 3 steps (Figure 4.2):

1. Firstly, the random forest algorithm is used to compute the probability of a pixel to belong or not to the segmented tissue. The training data is manually selected by the user and include state and space characteristics as: voxel grey intensity, voxel's neighbors intensity (with variable radius of neighboring), (x; y; z) voxel position (Figure 4.2.c).
2. Secondly, spherical seeds point with variable radius are placed on the new synthetic volume to mark the connected components bellowing to the segmented tissue (Figure 4.2.d).
3. Finally, the placed seed point will evolve in the 3D space with a speed and direction driven by the pixel intensity and sign in the synthetic volume (Figure 4.2.e).

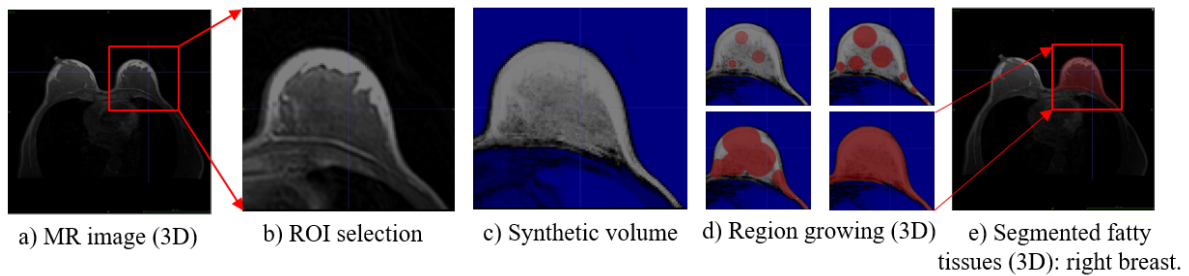


Figure 4.2: Breast tissues segmentation on the breast MRI of the second subject. Prone breast configuration. White-voxel belongs to breast tissue; blue - voxel don't belongs to fatty tissue

After segmentation, an additional manual correction was performed to refine components boundaries. Simple erosion and dilatation operations were applied on breast and muscle segmented volumes in order to obtain smoother connected components. Then to avoid tissues overlapping at muscle-breast juncture border binary operations were used.

The process was repeated for both volunteers and for each breast configuration: supine, prone and supine tilted.

4.2.3 Image registration

During the imaging acquisition process, the subject is moved in and out the MRI scanner. Therefore, the breast not only undergone an elastic transformation, but also a rigid one. Prior to image acquisition, four landmarks are fixed on the chest wall. The landmarks are placed on sternum and inframammary fold lines, regions known to be rich in fibrous ligaments limiting the soft tissues elastic deformation. To assess the body position changes

between the two configurations a rigid transform is computed by minimizing the Euclidian
 1185 distance of the four points defined by the four landmarks. The transformation is estimated
 using the iterative closest point (ICP) algorithm proposed by ITK library.

However, because of breast hyperelasticity the computed transformation is not accurate
 enough. Therefore, a second registration step is performed by aligning the bone structures
 1190 of the anterior part of thoracic cage from prone and supine tilted positions to the supine
 one. The muscular tissues mask previously segmented are used in order to remove body
 soft tissues. The image registration is implemented using the descendant gradient based
 algorithm minimizing the images cross correlation (ITK library).

Figure 4.3 shows overlapping prone-supine and supine tilted-supine breast images in
 the transversal plane after registration. the anterior part of the chest line is wall aligned,
 1195 however there are some differences because of elastic thoracic cage deformation due to hand
 positions or body-mass force reparations.

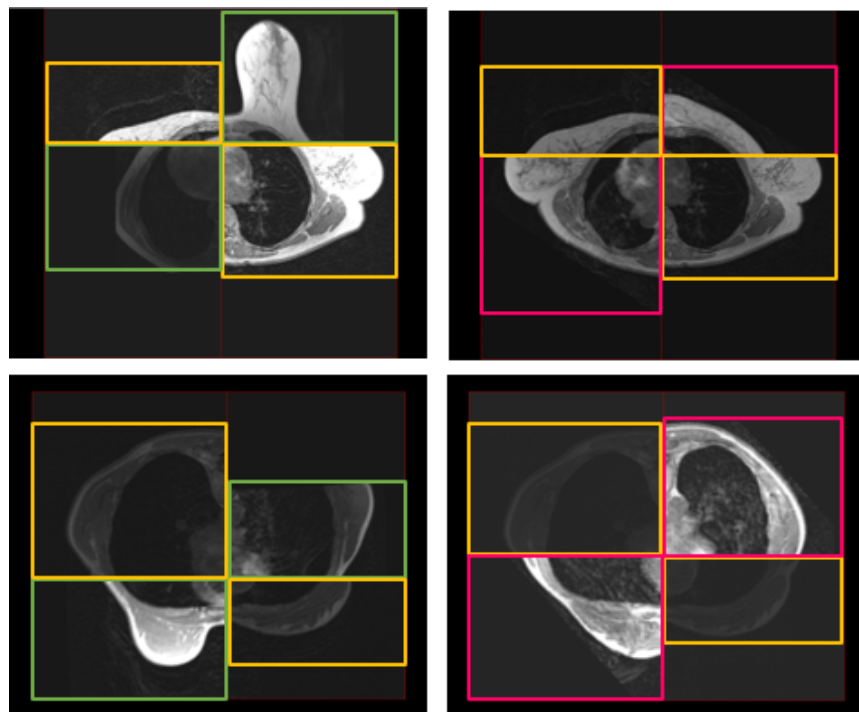


Figure 4.3: Registered MRI images: first line- subject 1; second line- subject 2; first column - prone configuration versus supine; second column - supine tilted versus supine

In a multi-gravity loading simulation, the force of gravity is applied to the whole model
 as a body force. It can be broken down into three components of the Cartesian coordinate
 system labeled X, Y, and Z. The supine configuration was chosen as a reference state,
 1200 therefore the gravity loading direction was set to be oriented on the inverse direction of
 the Z axis (postero-anterior direction): $\gamma_s = (0, -1, 0)$. The gravity loading direction
 for the two other positions are given by the rigid transformation computed by images
 registration: $\gamma_p = (0.037, 0.985, -0.165)$ direction vector for gravity in prone position and

$\gamma_{st} = (-0.744, -0.667, 0.023)$ direction vector for supine tilted position.

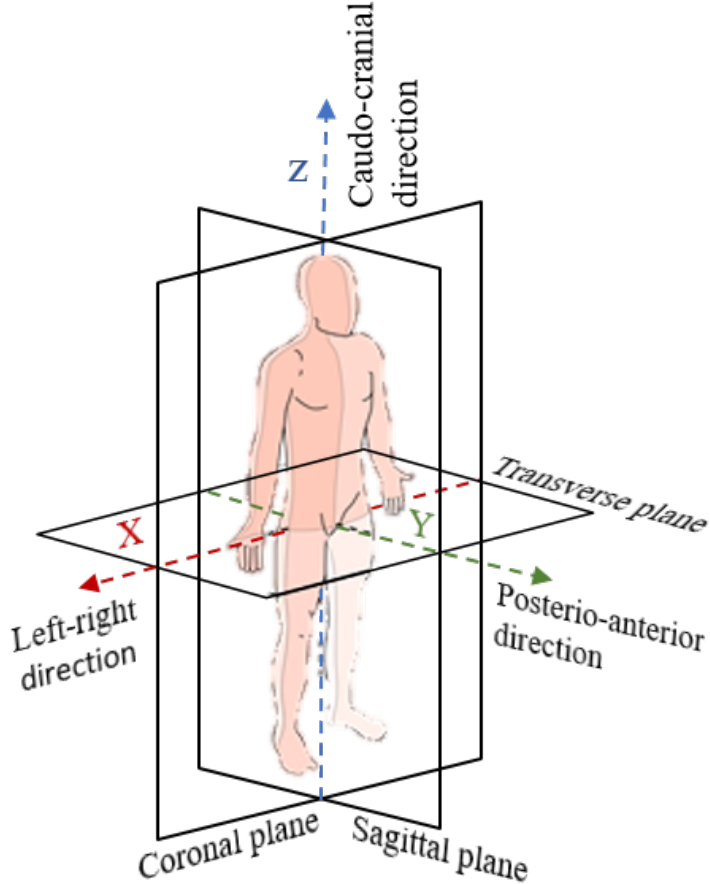


Figure 4.4: Anatomical planes and nominal Cartesian axis directions.

¹²⁰⁵ 4.3 Breast geometry and Finite Elements Mesh

The biomechanical breast model was created based on the breast MR images of the second subject. Following image segmentation, two surface meshes were created. The first one represents the contours of breast tissue and the second one represents the thoracic cage and muscle contours (Figure 4.5.b). We used a the semi-automatic Skin Surface module proposed by SpaceClaim Direct Modeler to convert the mesh surfaces to NURB surfaces 4.5.c).

The 3D geometries were meshed using ANSYS Mechanical Software with 4 nodes tetrahedra (solid285) in a mixed U-P formulation. The breast skin is modeled as a 2mm thick single layer of shell elements. Shell elements and the underlying breast elements are sharing the same nodes.

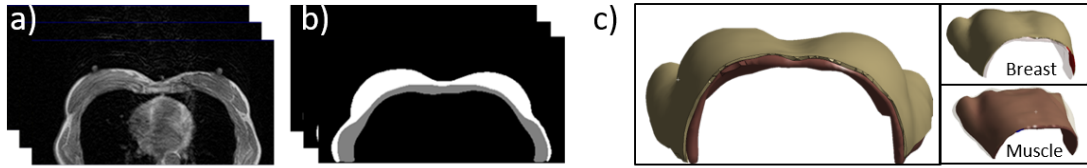


Figure 4.5: 3D geometries generation. a) MR images; b) segmented image; c) corresponding 3D geometries

Thanks to a sensibility analysis, the appropriate mesh size was chosen such as the displacement results will be affected by the lower mesh resolution by less than 5%. This can be verified by running several simulations on the same breast model with several different mesh densities.

1220 **insert displacement vs mesh density figure**

This constraint resulted in elements sizes ranging between 7 and 10mm. The mesh that was chosen consists in 18453 tetrahedral elements and 1980 shell elements. The tetrahedral mesh consists of 9625 elements assigned to the pectoral muscle and the toracic cage and 1225 8828 elements assigned to breast tissues.



Figure 4.6: Finite elements mesh components. The tissues components are cropped for visualization purposes.

Elements quality is measured using three criteria: element skewness, aspect ratio and maximal corner angle. The Figure 4.7 shows values ranges of elements shape parameters. The element's aspect ratio and maximal corner angle range between the nominal limits defining a good mesh quality (Section [refsubsection:lagrangianmesh](#)). There are a small number of elements with a skewness larger than 0.75, however there are no degenerated elements (skewness =1).

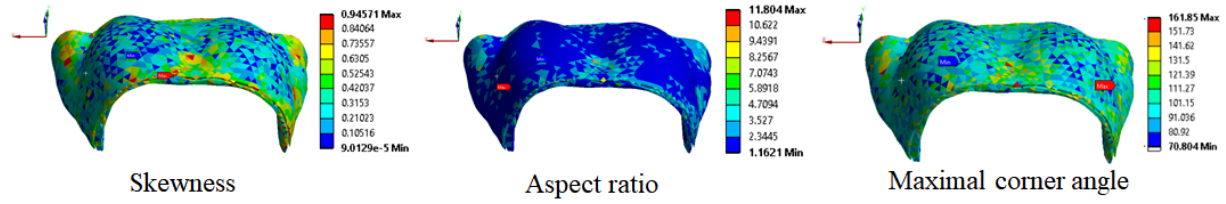


Figure 4.7: Finite elements mesh quality.

4.4 Breast stress-free geometry

To estimate the stress-free configuration of the breast, an adapted prediction-correction iterative approach was implemented. Prone and supine image data sets are used to compute the stress-free geometry. The overall iterative process is presented in Figure 5.1. The first estimate of stress-free breast configuration is obtained by inverse gravity on supine geometry. Then, at each iteration, the estimated stress-free configuration is used to simulate breast deformation due to gravity in a prone position. The differences between result of this simulation and the real shape of the breast in prone position is quantified by computing the Euclidian distance D_i between the *active nodes* defined at the breast external surface. This distance is then used in the next iteration of our process to simulate an imposed displacement (Dirichlet condition) to the active node i in the stress-free condition. To limit any mesh distortion, the displacement is only partially imposed using a multiplicative regularization factor ($\lambda < 1$). The process repeats as long as the new transformation improves the similarity between two geometries by more than 1mm on average. The similarity between the estimated and measured prone breast configuration is given by the mean Euclidean distance over the active nodes.

To compute the node-to-node distance D_i , the active nodes position on prone configuration have to be known. Thus, an additional mesh registration step is performed at each iteration. The active nodes are morphed into prone configuration using the elastic deformation method proposed by Bucki et al. (2010). The method estimates a C1-diffeomorphic, non-folding and one-to-one transformation to register a source point cloud onto a target data set D, which can either be a point cloud or a surface mesh. The input source points set is initially embedded in a deformable virtual hexahedral elastic grid. Then an iterative registration technique is performed by successive elementary grid deformations and at different grid refinement level.

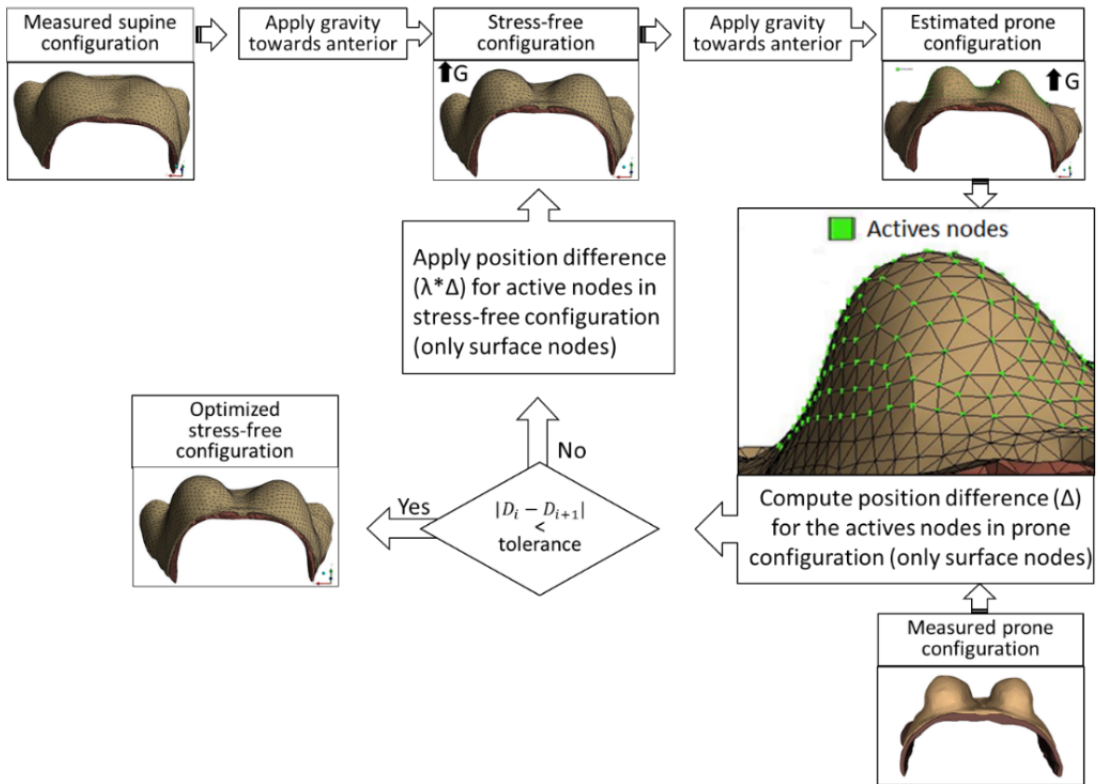


Figure 4.8: Fixed point type iterative algorithm for stress-free geometry approximation. D_i - mean node to node distance over the active nodes at iteration i , G - gravity force

4.5 Boundary conditions

- Explain the boundary conditions with a bonded contact surface: give the obtained results with materials model from bibliography
- Explain the boundary conditions with sliding boundary conditions
- Explain the mechanical and computational role of fascia
- Explain the mechanical and computational role of ligaments.

The breast fascial system and the suspensory ligaments is modeled by adding new membranous structures in the finite element mesh. Superficial layer of superficial fascia is integrated in the skin layer. In addition, a new layer of 0.1mm thick shell elements is added at the juncture surface between muscle and breast tissue to model the deep layer of the superficial fascia. Shell elements and the underlying breast elements are sharing the same nodes. Since the deep fascia and muscle tissues are supposed to present similar elastic properties, the deep fascia is not explicitly modeled.

As mentioned earlier, the breast is firmly attached to the deep fascia via suspensory ligaments but moves freely over the pectoralis muscle. We therefore introduced a contact surface between the posterior breast face and the anterior muscle face (Figure 4.9). For

this, we use the no-separation contact model from ANSYS Contact Technologies with a friction coefficient (k) equal to 0.2. The penalty method is used as a contact algorithm with ANSYS default values to control gap and penetration tolerance factors. The opening stiffness factor as well as the normal and tangential stiffness factors are adapted for each simulation case in order to ensure the solution convergence.

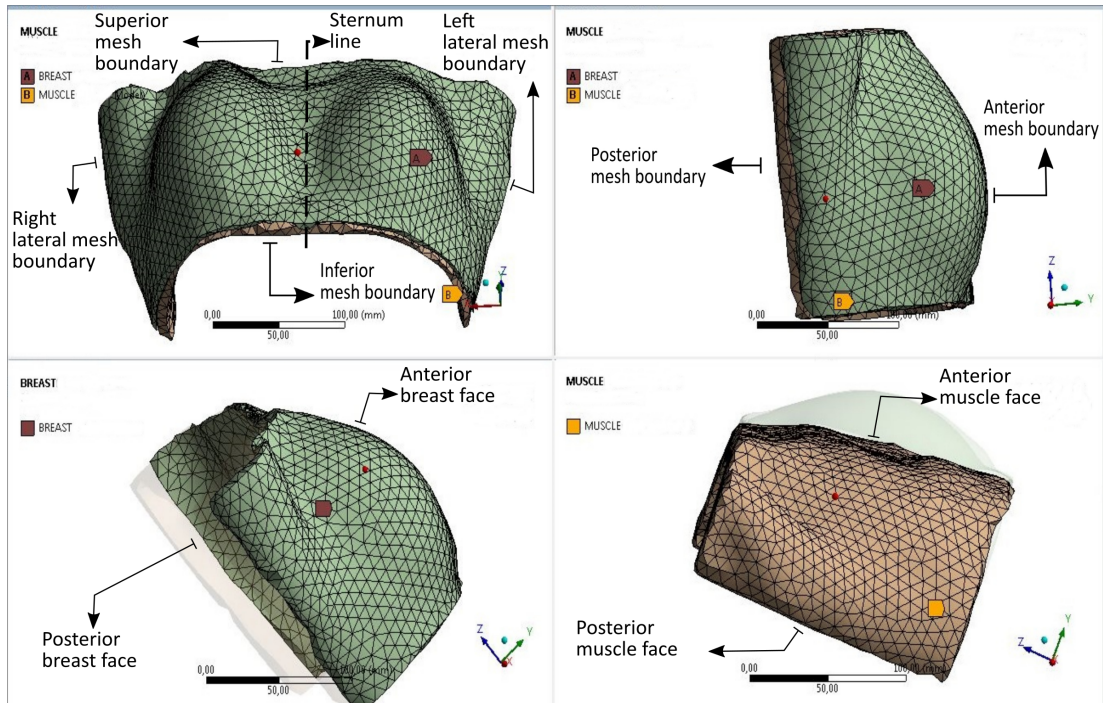


Figure 4.9: Finite elements mesh boundaries

Dirichlet boundary conditions are added to posterior face of the pectoral muscle (figure 4.9). Superior and inferior ends of the deep fascia layer are constrained in Z direction; superior and inferior ends of skin layer are constrained in Y direction. For left and right lateral breast boundaries (Figure 4.9), Dirichlet conditions are too strong and preclude breast tissue to slide laterally. Therefore, in these regions ligamentous structures are included with a cable-like behavior. All ligamentous structures: inframammary ligament, deep medial ligament and lateral ligaments are modeled using Ansys link type elements connecting breast posterior surface nodes to anterior muscle surface nodes (Figure 7). Consequently, the sliding range is controlled only by the initial state of the link elements and by the stiffness of the deep fascial layer.

4.6 Materials constitutive models

The proposed model consider of 6 types of tissues, wherein 4 tissues (glandular, fatty, muscle and skin) are well described and regularly used for biomechanical modeling and

2 of them (fascia and suspension ligaments) with limited used and poorly described in literature.

To fine-tune the searching intervals of each constitutive parameter, a sensitivity analysis is performed. Based on existing publications, an interval of possible values is defined for each material (Table 1). Within these intervals, the values of the elastic parameters were incremented one by one by steps of 10%. Results of the corresponding simulations are shown on Figure 10. The first column represents the variation of mean node displacement together with the maximal node displacement for a given parameter set. The second column represent the maximal difference in nodal displacement between two consecutive simulations (change rate); and the maximal difference in node displacement between the actual and the less deformed geometry (cumulative change rate). The change rate is computed within the assumption that the maximal displacement over the simulations set is equal to 100% change rate

Subject specific mechanical tissue properties are computed using an optimization process based on a multi-gravity loading simulation procedure. First, for a given set of parameters (E_{breast} , E_{muscle} , E_{skin} , E_{fascia}) the breast stress-free configuration is estimated by minimizing the difference between the simulated and measured breast geometry in prone configuration. Then, from the new estimated stress-free geometry, the supine breast configuration is computed and the new estimated geometry is compared to the measured one using modified Hausdorff distance (Dubuisson, M-P and Jain, Anil K 1994). To avoid taking in account the geometry dissimilarity due to arms position, the modified Hausdorff distance is computed only on breast skin surface. In this process multiple simulation based on imposed displacement are performed, therefore the FE mesh can be significantly altered before reaching an optimal stress-free geometry. Mainly for that reason we chose to perform an exhaustive manual rather than an automatic research of the optimal set of constitutive parameters.

One can see that the model is very sensitive to the variation of Youngs modulus of breast tissue, skin and fascia. However, beyond some values of the constitutive parameters, materials become too stiff and do not change significatively under gravity loadings. Therefore, the search intervals for breast tissue and skin Youngs modulus have been reduced such that a larger value will impact the cumulative change rate less than 20% (max displacement less than 5mm), i.e. 0-4 kPa, 0-20 kPa respectively. As the fascia stiffness governs the lateral displacement only a threshold of 10 % (2.5mm) have been chosen, i.e. the search interval ranging between 0-250 kPa. The new defined intervals are discretized by steps of 0.1 kPa, 1kPa and 40 kPa. The discretization step has been chosen such that the change rate between two consecutive simulations is less than 10%.

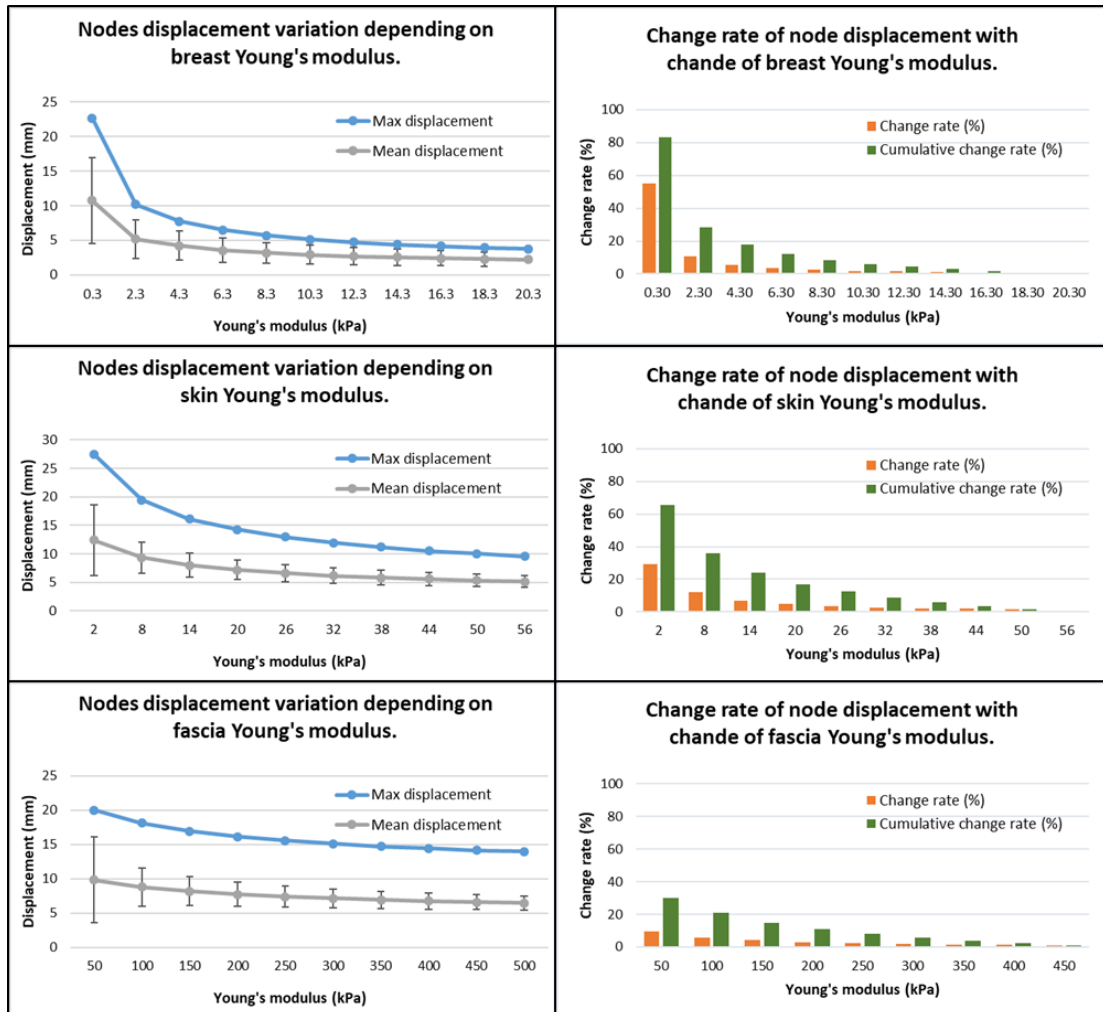


Figure 4.10: First column: relation between maximal and mean nodes displacement and the equivalent Young's modulus variation for different tissues. Second column: rate and cumulative change rate of node displacement in function of quivalent Young's modulus

Model validation

1330 5.1 Technical approach

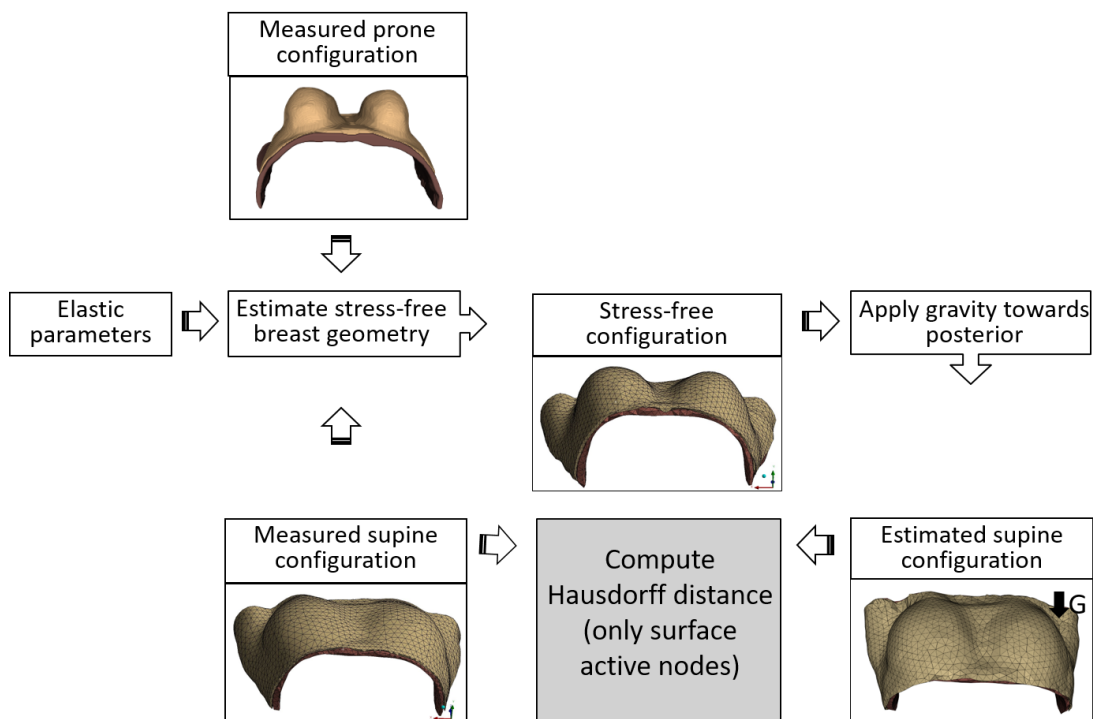


Figure 5.1: Process to estimate optimal material parameters

5.2 Results

Add the results with Gent model and compare

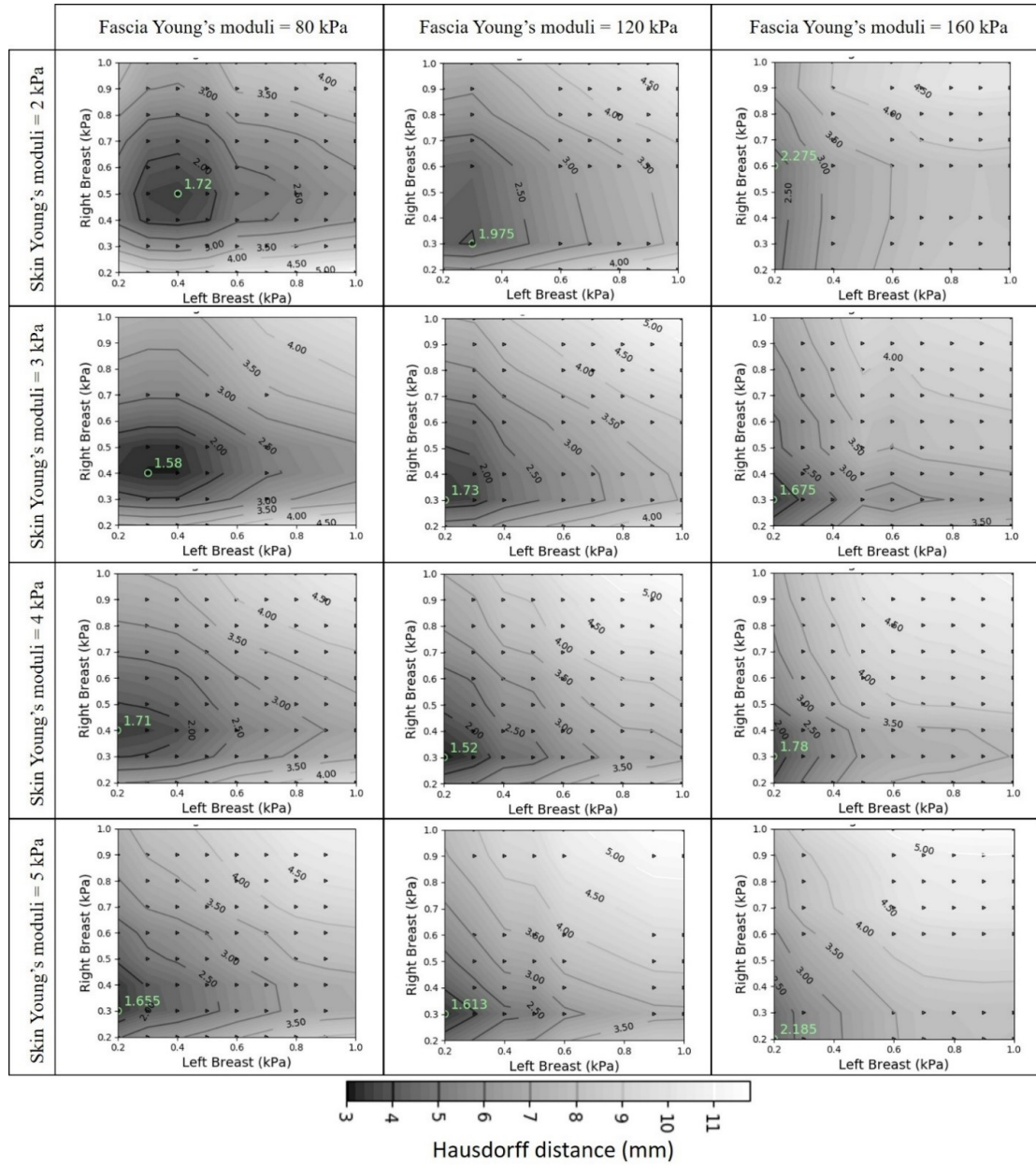


Figure 5.2: Hausdorff distance on the skin surface over the constitutive parameters space

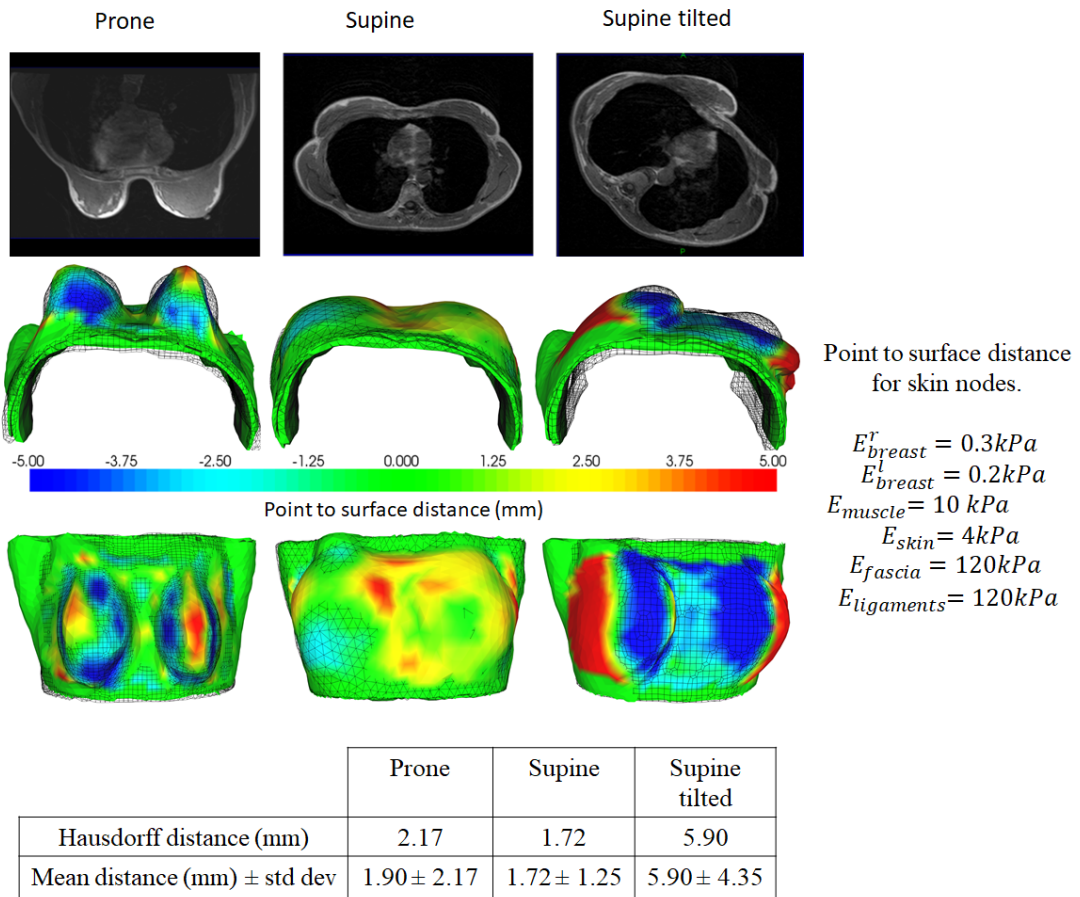


Figure 5.3: Three breast configurations: prone, supine and supine tilted. First line - MR images in 3 breast configurations. Second and third lines - point to node distance from simulated breast shape (surface mesh) to the measured one (black grid lines).

5.3 Discussions and conclusion

Part III

Breast Compression: a comparative study

Background

6.1 Introduction

1340 The scope of this work is to assess the differences in terms of patient comfort, image quality and patient dose exposure when using a rigid or a flex paddle. Several studies showed that, the pain experienced by women during the mammographic exam depends on psychologic factor⁵ (technician behavior, patient anxiety), sociologic factors⁶ (ethnicity, education level) as well as physiologic⁷ factors (compression level, breast size). Here,
1345 the psychologic and sociologic factors are neglected. The study focuses on physiological factors as the compression force or structural specifications of the compression paddle to characterize the patient comfort.

In this purpose, MR images of two subjects are used to create patient specific finite elements breast models. The mechanical behavior of soft tissues under compression is
1350 computed for both subjects and for both paddle designs. The perceived pain for a given paddle design is quantitatively characterized by contact pressure, internal stress and strain distributions. After compression, three sets of macrocalcifications are inserted into breast volumes. The latter are then subject to a Monte-Carlo based simulation (CatSim⁸) enabling to simulate the image acquisition of the compressed breast with a mammography system.
1355 Then, the diagnosis quality is assessed by measuring the signal-difference-to-noise-ratio (SDNR), signal-to-noise-ratio (SNR) and the average glandular dose (AGD).

6.2 Breast compression: overview

-Describe breast positioning and compression (Groot)
-Describe today's compression standards: force-thickness relation; thickness- AGD; force/thickness and pain relation; Pressure standardized mammography.
1360

6.3 Compression paddle designs

During mammography, a qualified radiologic technologist positions the breast of the patient between a stationary image receptor and a movable paddle (Figure 3). The technologist

gradually compresses the breast in order to even out the breast thickness and to spread out
 1365 the soft tissues. Nowadays, two types of compression paddles are widely available: rigid
 compression paddles (RCP) and flex compression paddles (FCP).

The RCP is fixed to its frame and is constrained to move in the up-down direction.
 This paddle has some flexibility because of material mechanical properties and can slightly
 1370 bend when compressing the breast, while remaining globally flat and parallel to the image
 receptor. On the other hand, the FCP is attached to its frame by rotational joints and
 therefore, presents an additional rotational degree of freedom enabling the paddle to tilt
 with respect to the image receptor plane (Figure 3.c).

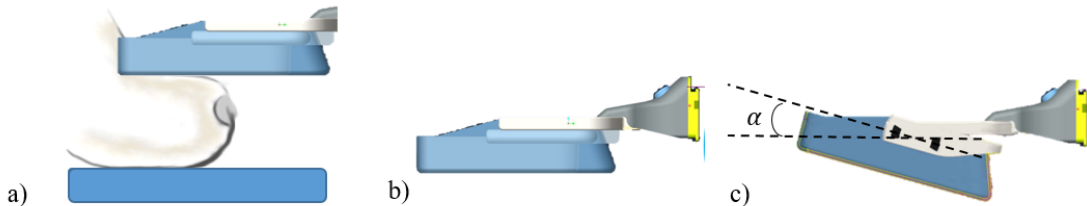


Figure 6.1: Breast compression between the paddle (up) and the receiver (down): a) Rigid paddle; b) Flex paddle with flexion angle α

6.4 Discussions and Conclusion

¹³⁷⁵ Breast compression quality evaluation

7.1 Compression paddles FE models

7.2 Compressure quality metrics

7.2.1 Patient comfort

With a rigid paddle, the breast under compression presents a nearly uniform thickness all over the contact surface. Contrariwise, with a flex paddle, the compressed breast thickness decreases quasi linearly from the chest wall to the nipple. Flex paddles are used to better conform the breast contours and thereby to improve compression. However, Broeders and colleagues¹¹ have shown that such compression paddle may decrease the diagnostic quality of mammograms as the breast tissues may be pushed out to the chest wall resulting in less retro-glandular tissue visible on the image.

7.2.2 Image quality

To assess the impact of breast compression on image quality, we inserted a set of microcalcifications into each compressed breast volume. The smallest breast volume contains 21 microcalcifications arranged in a matrix of 7 rows and 3 columns (Figure 4a). The largest breast volume contains 56 microcalcifications arranged in a matrix of 7 rows and 8 columns. The matrix of calcifications is parallel with the entrance surface of the image receptor and positioned at the breast mid thickness (Figure 4b). The distance between two consecutive columns or rows is 10mm. We assumed a uniform breast-equivalent material composed of glandular/adipose tissue with a 20/80 ratio. A mammogram was simulated using typical clinical acquisition parameters obtained with the standard automatic optimization of parameters (AOP) mode. Two simulations were performed with microcalcifications of 0.2 mm and 0.3mm in diameter. The signal-difference-to-noise ratio (SDNR) per pixel of these microcalcifications was measured. Additionally, the signal-to-noise ratio (SNR) was computed on the same pixels excluding the microcalcifications.

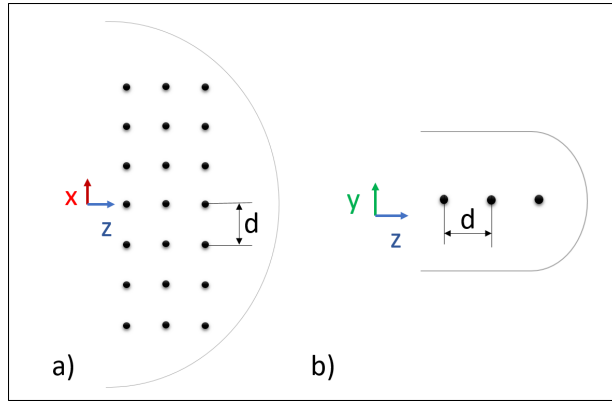


Figure 7.1: Microcalcification distribution over the smallest breast volume ($d = 10\text{mm}$): a) axial view, b) sagittal view.

¹⁴⁰⁰ 7.2.3 Average glandular dose

The average glandular dose (AGD) was derived using the approach proposed by Dance et al¹² regardless the paddle type. In practice, it is very difficult to accurately measure the exact breast thickness. Thus, the nominal breast thickness was used to compute conversions factors which relate measurements of incident air kerma to the delivered mean glandular dose.

¹⁴⁰⁵

7.3 Results

The force versus breast thickness curves are plotted in Figure 5 for both volunteers with the rigid and flex paddles. We observed a nominal compression thickness roughly equals for both paddles. The resulting internal stress and strain distributions, as well as contact pressure maps were derived at compressive forces of 22 N for the first volunteer (Figure 6) and 95 N for the second one (Figure 7).

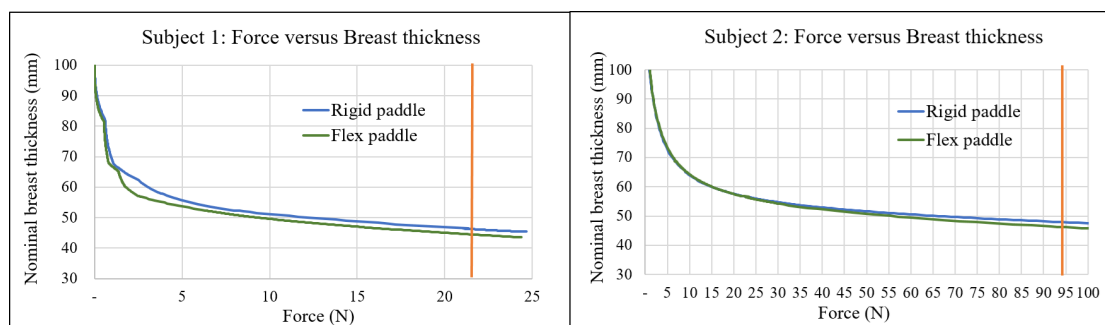


Figure 7.2: Resulting breast thickness for a given compression force

As concerns the small breast volume (Figure 6), there is no significant difference between FCP and RCP in pressure distribution over the skin surface or in internal stress/strain in-

tensity distributions. For both compression paddles, high pressure at the skin surface is
1415 concentrated in the juxtathoracic region with a maximum pressure of 77.7 kPa. Several clinical studies^{11,13} sustained this result of no significant difference in experienced pain when using FCP or RCP. In addition, the FE simulations confirm that in small breasts the paddle tilt is too small to impact the tissues compression in the middle part of the breast. FCP applied on large breast volumes (Figure 7) results in significantly lower intensities of pressure at the skin surface in contact with the compression paddle, with a maximal pressure of 37 kPa, compared to 56 kPa when using RCP. No significant difference in the measured maximal intensities of strain and stress was observed, however strain and stress distribution patterns are different. When the breast is compressed with a rigid paddle, maximal strain and stress are concentrated in the retromammary space and de-
1420 crease considerably toward the nipple. When a flex paddle is used, stress and strain are more uniformly distributed over the breast volume with the highest values in the middle third of the breast. The areal pressure distribution patterns has already been demonstrated in the work by Dustler and colleagues¹³. The authors have studied the pressure distribution patterns of 103 women undergoing breast compression with a rigid paddle at different compression levels. Four groups have been differentiated: a) skin pressure widespread over the breast (29%); b) skin pressure concentrated on the central part of the breast (8%); c) skin pressure concentrated on the juxtathoracic region (16%); d) skin pressure concentrated along a narrow zone at the juxtathoracic region (26%). The pressure distribution patterns observed for our first and second volunteers correspond to the group d and a respectively.
1425

The nominal breast thickness may vary by about 2mm between rigid and flex paddle for both volunteers (Table 3). Accordingly, no significant difference was found between the estimated AGD, while a dose reduction of 2% for the smaller breast and 4% for larger breast was observed.

The SNR and SDNR have been estimated and compared between flex and rigid paddles.
1430 When using a flex paddle instead of a rigid paddle on the largest breast (volunteer 2), we observe a statistically significantly higher SNR. The same trend is observed on SDNR for both 200 and 300 m microcalcifications, while not statistically significant. We did not observe any statistically significant difference in SNR or SDNR for microcalcification of any size when considering the compression of the smallest breast by a rigid or a flex paddle.
1435 Therefore, despite a breast thickness varying linearly from chest wall to nipple when the flex compression paddle is used, the image quality is preserved or improves compared to the image quality obtained with the rigid compression paddle.

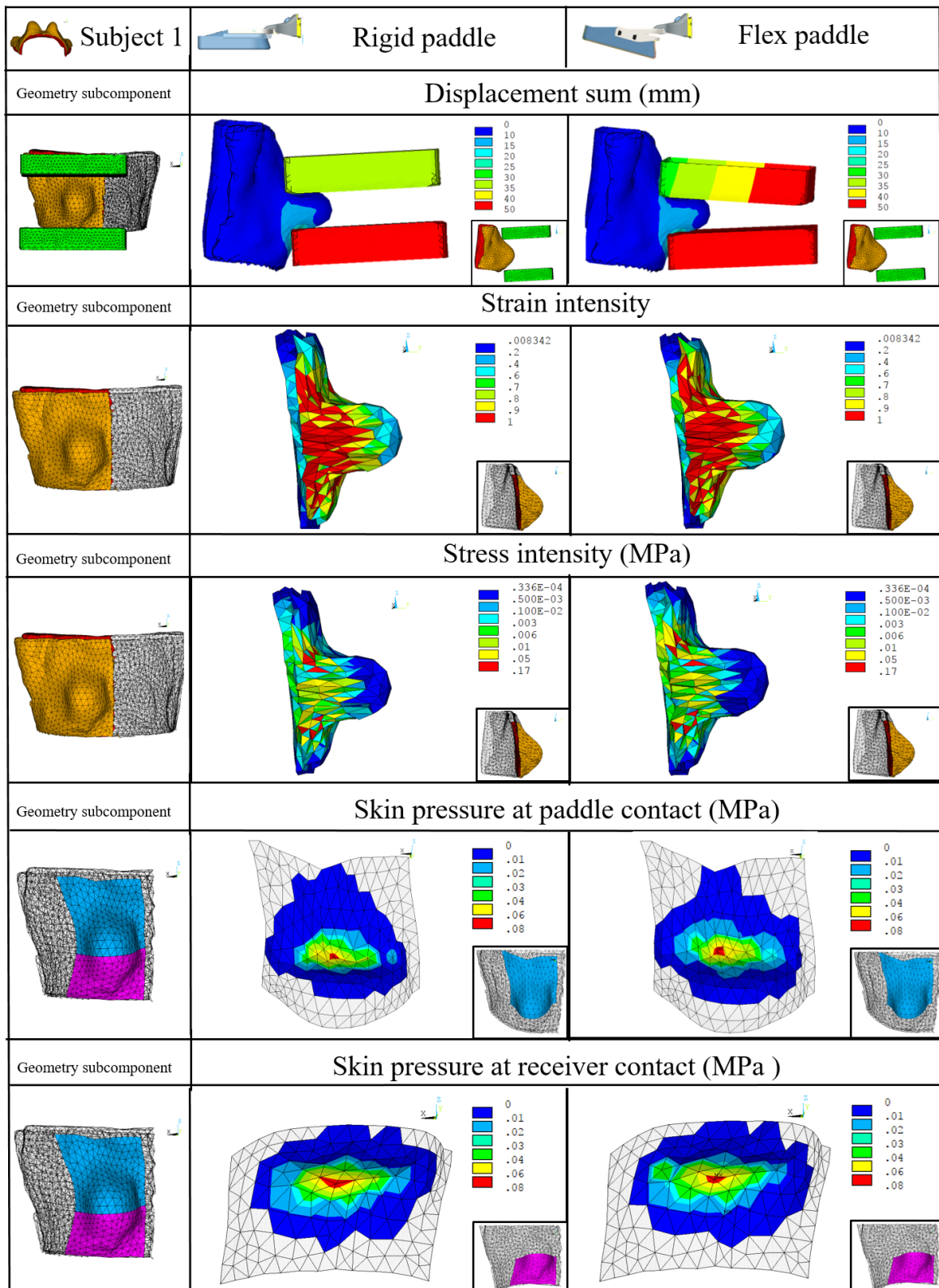


Figure 7.3: Stress, strain and contact pressure distribution for the first subject

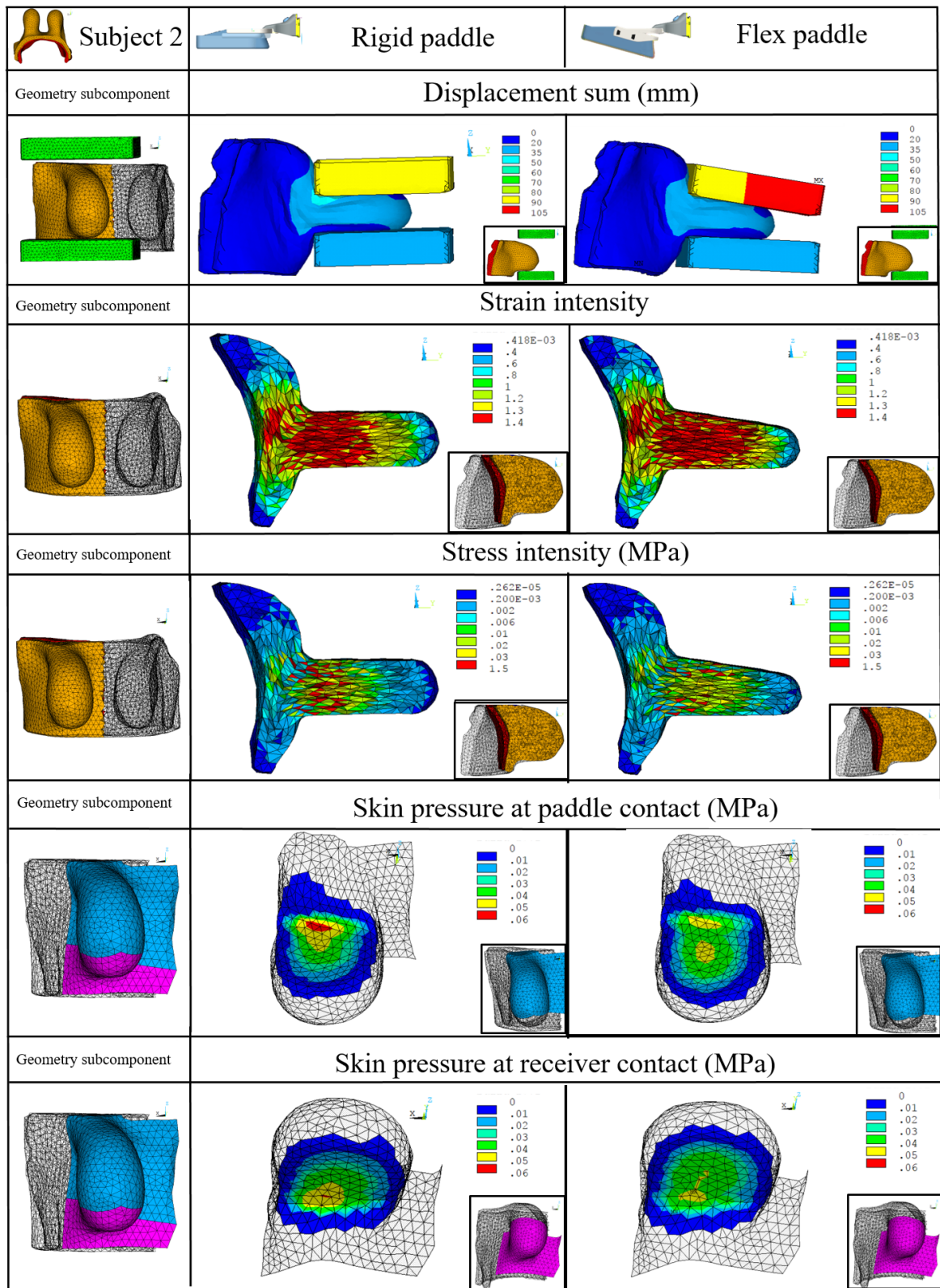


Figure 7.4: Stress, strain and contact pressure distribution for the second subject

	Rigid Paddle		Flex Paddle		p-Values	Rigid Paddle		Flex Paddle	
	Mean SNR	StdDev SNR	Mean SNR	StdDev SNR		BNT (mm)	AGD (mGy)	BNT (mm)	AGD (mGy)
Volunteer 1	82,90	43,09	83,70	37,72	0,706	46	1,15	44	1,12
Volunteer 2	126,89	8,75	137,21	10,73	0,000	48	1,20	46	1,15

	200 um				300 um					
	Rigid Paddle		Flex Paddle		Rigid Paddle		Flex Paddle			
	Mean SDNR	StdDev SDNR	Mean SDNR	StdDev SDNR	p-Values	Mean SDNR	StdDev SDNR	Mean SDNR	StdDev SDNR	p-Values
Volunteer 1	0,74	0,68	0,79	0,54	0,689	2,01	1,28	1,85	1,02	0,224
Volunteer 2	1,14	0,57	1,13	0,53	0,885	2,96	0,76	3,15	0,92	0,093

Figure 7.5: Breast nominal thickness (BNT), average glandular dose (AGD), signal-to-noise-ratio (SNR) and signal-difference-to-noise (SDNR) for both volunteers and both compression paddle types

7.4 Discussions and conclusion

Breast compression with flex and rigid paddle have been simulated using the finite elements theory applied to segmented MRI images acquired on 2 volunteers under different geometries. Applying the Gent form of strain-energy potential, instead of the Neo-Hookean form, allowed to obtain compression force magnitudes comparable with the real subject data. After simulating the breast compression, the SDNR of microcalcifications and the AGD, delivered during the acquisition of the corresponding simulated mammography, have been computed. The simulations have been repeated for two different breast volumes (cup sizes A and F) with a rigid and a flex paddle. The four configurations have been analyzed to compare patient perceived pain (measured as strain and stress) and image quality (measured as SNR, SDNR and AGD). The results of our simulations indicate that, for the smallest breast, there is no significant difference for the patient perceived pain when using the rigid or the flex paddle. The shape of the breast under compression does not present significant changes between the two paddle designs. We did not observe any statistically significant difference in SNR or SDNR for microcalcification of any size when considering the compression of the smallest breast by a rigid or a flex paddle. Therefore, our results suggest that using a flex paddle should not significantly impact image quality and delivered dose in small breasts, and should not reduce significantly the perceived pain. For the largest breast, our simulations indicate that using a flex paddle may reduce the maximal pressure intensity on the skin surface by about 30% compared to the rigid paddle. The tissues deformation is more uniformly distributed inside the breast volume, and the highest deformation is occurring in the middle breast region corresponding to the supposed location of dense tissues. Moreover, our simulations have shown that flex paddle have no significant impact on the average glandular dose and improves image quality compared to the rigid paddle. In conclusion, our simulations confirm that using the flex paddle used for breast compression may improve the patient comfort without affecting the image quality and the delivered average glandular dose. Moreover, despite a breast thickness varying linearly from chest wall to nipple, when a flex compression paddle is used on large breasts, the image quality seems to be preserved or improved compared to the image quality obtained with a rigid compression paddle

Part IV

Thesis review

General conclusion and perspectives

8.1 Conclusion

8.2 Perspective

22

Bibliography

- Abu-Hijleh, M., Roshier, A., Al-Shboul, Q., Dharap, A., and Harris, P. (2006). The membranous layer of superficial fascia: evidence for its widespread distribution in the body. *Surgical and Radiologic Anatomy*, 28(6):606–619. 9
- 1490 ACS (2017). American cancer society: Types of breast cancer. <https://www.cancer.org/cancer/breast-cancer/understanding-a-breast-cancer-diagnosis/types-of-breast-cancer.html>. 11, 12
- Andolina, V. and Lillé, S. (2011). *Mammographic imaging: a practical guide*. Lippincott Williams & Wilkins. 8, 9, 10, 11
- 1495 Andrews, F. J. (2001). Pain during mammography: implications for breast screening programmes. *Journal of Medical Imaging and Radiation Oncology*, 45(2):113–117. 15
- Aro, A. R., De Koning, H. J., Absetz, P., and Schreck, M. (1999). Psychosocial predictors of first attendance for organised mammography screening. *Journal of Medical Screening*, 6(2):82–88. 15
- 1500 Azar, F. S., Metaxas, D. N., and Schnall, M. D. (2002). Methods for modeling and predicting mechanical deformations of the breast under external perturbations. *Medical Image Analysis*, 6(1):1–27. 40, 42, 45
- Bayati, S. and Seckel, B. R. (1995). Inframammary crease ligament. *Plastic and reconstructive surgery*, 95(3):501–508. 8
- 1505 Bucki, M., Lobos, C., and Payan, Y. (2010). A fast and robust patient specific finite element mesh registration technique: application to 60 clinical cases. *Medical image analysis*, 14(3):303–317. 52
- Carter (2009a). *Determining material properties of the breast for image-guided surgery*. International Society for Optics and Photonics. 41, 42
- 1510 Carter, T., Han, L., Taylor, Z., Tanner, C., Beechy-Newman, N., Ourselin, S., and Hawkes, D. (2012). Application of biomechanical modelling to image-guided breast surgery. *Soft Tissue Biomechanical Modeling for Computer Assisted Surgery*, pages 71–94. 40

BIBLIOGRAPHY

- Carter, T. J. (2009b). *Biomechanical modelling of the breast for image-guided surgery*. PhD thesis, University of London. 38, 39, 40, 41, 42, 43
- 1515 Catanuto, G., Spano, A., Pennati, A., Riggio, E., Farinella, G. M., Impoco, G., Spoto, S., Gallo, G., and Nava, M. B. (2008). Experimental methodology for digital breast shape analysis and objective surgical outcome evaluation. *Journal of Plastic, Reconstructive & Aesthetic Surgery*, 61(3):314–318. 6
- 1520 Chan, H.-P., Galhotra, S., Vyborny, C. J., MacMahon, H., Jokich, P. M., et al. (1987). Image feature analysis and computer-aided diagnosis in digital radiography. i. automated detection of microcalcifications in mammography. *Medical physics*, 14(4):538–548. 13
- Cheung, J. T.-M., Zhang, M., and An, K.-N. (2004). Effects of plantar fascia stiffness on the biomechanical responses of the ankle–foot complex. *Clinical Biomechanics*, 19(8):839–846. 43
- 1525 Ciocca, D. R. and Fanelli, M. A. (1997). Estrogen receptors and cell proliferation in breast cancer. *Trends in Endocrinology & Metabolism*, 8(8):313–321. 11
- Clemente, C. D. (2011). *Anatomy: a regional atlas of the human body*. Wolters Kluwer-/Lippincott Williams & Wilkins Health. 6, 8
- 1530 Conley, R. H., Meszoely, I. M., Weis, J. A., Pheiffer, T. S., Arlinghaus, L. R., Yankeelov, T. E., and Miga, M. I. (2015). Realization of a biomechanical model-assisted image guidance system for breast cancer surgery using supine mri. *International journal of computer assisted radiology and surgery*, 10(12):1985–1996. 38
- Dullum, J. R., Lewis, E. C., and Mayer, J. A. (2000). Rates and correlates of discomfort associated with mammography. *Radiology*, 214(2):547–552. 15
- 1535 Eder, M., Raith, S., Jalali, J., Volf, A., Settles, M., Machens, H.-G., and Kovacs, L. (2014). Comparison of Different Material Models to Simulate 3-D Breast Deformations Using Finite Element Analysis. *Annals of Biomedical Engineering*, 42(4):843–857. 40, 41
- 1540 Eiben, B., Lacher, R., Vavourakis, V., Hipwell, J. H., Stoyanov, D., Williams, N. R., Sabczynski, J., Bülow, T., Kutra, D., Meetz, K., et al. (2016a). Breast conserving surgery outcome prediction: A patient-specific, integrated multi-modal imaging and mechano-biological modelling framework. In *International Workshop on Digital Mammography*, pages 274–281. Springer. 40
- Eiben, B., Vavourakis, V., Hipwell, J. H., Kabus, S., Buelow, T., Lorenz, C., Mertzanidou, T., Reis, S., Williams, N. R., Keshtgar, M., and Hawkes, D. J. (2016b). Symmetric Bio-mechanically Guided Prone-to-Supine Breast Image Registration. *Annals of Biomedical Engineering*, 44(1):154–173. 38

- Eiben, B., Vavourakis, V., Hipwell, J. H., Kabus, S., Lorenz, C., Buelow, T., and Hawkes, D. J. (2014). Breast deformation modelling: comparison of methods to obtain a patient specific unloaded configuration. *Proc. SPIE*, 9036:903615–8. 38, 39
- 1550 Eiben, B., Vavourakis, V., Hipwell, J. H., Kabus, S., Lorenz, C., Buelow, T., Williams, N. R., Keshtgar, M., and Hawkes, D. J. (2016c). Surface driven biomechanical breast image registration. In *SPIE Medical Imaging*, pages 97860W–97860W. International Society for Optics and Photonics. 43, 44, 45
- Fanelli, M. A., Vargas-Roig, L. M., Gago, F. E., Tello, O., De Angelis, R. L., and Ciocca, D. R. (1996). Estrogen receptors, progesterone receptors, and cell proliferation in human breast cancer. *Breast cancer research and treatment*, 37(3):217–228. 11
- 1555 Fleming, P., O'Neill, S., Owens, M., Mooney, T., and Fitzpatrick, P. (2013). Intermittent attendance at breast cancer screening. *Journal of public health research*, 2(2). 15
- FNAH (2016). Cancer du sein : modalités spécifiques de dépistage pour les femmes haut risque. https://www.has-sante.fr/portail/jcms/c_1740821/fr/cancer-du-sein-modalites-specifiques-de-depistage-pour-les-femmes-a-haut-risque. 12
- FRM (2017). Les chiffres du cancer du sein. <https://www.frm.org/cancer-du-sein/>. 11
- 1560 1565 Gamage, T. P. B., Boyes, R., Rajagopal, V., Nielsen, P. M. F., and Nash, M. P. (2012). Modelling prone to supine breast deformation under gravity loading using heterogeneous finite element models. In Poul M.F. Nielsen, Adam Wittek, and Karol Miller, editors, *Computational Biomechanics for Medicine*, pages 29–38. Springer New York. 41, 43, 45
- Garcia, E., Oliver, A., Diaz, O., Diez, Y., Gubern-Merida, A., Marti, R., and Marti, J. (2017). Mapping 3d breast lesions from full-field digital mammograms using subject-specific finite element models. In *SPIE Medical Imaging*, pages 1013504–1013504. International Society for Optics and Photonics. 40, 45
- 1570 1575 Gefen, A. and Dilmoney, B. (2007). Mechanics of the normal woman's breast. *Technology and Health Care*, 15(4):259–271. 42
- Georgii, J., Paetz, T., Harz, M., Stoecker, C., Rothgang, M., Colletta, J., Schilling, K., Schlooß-Vries, M., Mann, R. M., and Hahn, H. K. (2016). Simulation and visualization to support breast surgery planning. In *International Workshop on Digital Mammography*, pages 257–264. Springer. 42, 43, 45
- 1580 Govindjee, S. and Mihalic, P. A. (1998). Computational methods for inverse deformations in quasi-incompressible finite elasticity. *International Journal for Numerical Methods in Engineering*, 43(5):821–838. 39

BIBLIOGRAPHY

- Griesenauer, R. H., Weis, J. A., Arlinghaus, L. R., Meszoely, I. M., and Miga, M. I. (2017). Breast tissue stiffness estimation for surgical guidance using gravity-induced excitation. *Physics in Medicine and Biology*, 62(12):4756. 41, 43
- 1585 Han, L., Hipwell, J. H., Eiben, B., Barratt, D., Modat, M., Ourselin, S., and Hawkes, D. J. (2014). A nonlinear biomechanical model based registration method for aligning prone and supine mr breast images. *IEEE transactions on medical imaging*, 33(3):682–694. 40, 42, 43, 45
- 1590 Han, L., year, J. H., Tanner, C., Taylor, Z., Mertzanidou, T., Jorge Cardoso, Sebastian Ourselin, and David J Hawkes (2012). Development of patient-specific biomechanical models for predicting large breast deformation. *Physics in Medicine and Biology*, 57(2):455–472. 38, 40, 41, 42
- 1595 Hendriks, F., Brokken, D., Oomens, C., Bader, D., and Baaijens, F. (2006). The relative contributions of different skin layers to the mechanical behavior of human skin in vivo using suction experiments. *Medical engineering & physics*, 28(3):259–266. 42
- Hofvind, S., Geller, B., Skelly, J., and Vacek, P. (2012). Sensitivity and specificity of mammographic screening as practised in vermont and norway. *The British journal of radiology*, 85(1020):e1226–e1232. 13
- 1600 Huang, S.-Y., Boone, J. M., Yang, K., Packard, N. J., McKenney, S. E., Prionas, N. D., Lindfors, K. K., and Yaffe, M. J. (2011). The characterization of breast anatomical metrics using dedicated breast ct. *Medical physics*, 38(4):2180–2191. 7
- Itoh, A., Ueno, E., Tohno, E., Kamma, H., Takahashi, H., Shiina, T., Yamakawa, M., and Matsumura, T. (2006). Breast disease: clinical application of us elastography for diagnosis. *Radiology*, 239(2):341–350. 14
- 1605 Kanitakis, J. (2002). Anatomy, histology and immunohistochemistry of normal human skin. *European journal of dermatology: EJD*, 12(4):390–9. 8
- Kellner, A. L., Nelson, T. R., Cervino, L. I., and Boone, J. M. (2007). Simulation of mechanical compression of breast tissue. *IEEE Transactions on Biomedical Engineering*, 54(10):1885–1891. 38
- 1610 Kemp Jacobsen, K., O'meara, E. S., Key, D., SM Buist, D., Kerlikowske, K., Vejborg, I., Sprague, B. L., and Lynge, E. (2015). Comparing sensitivity and specificity of screening mammography in the united states and denmark. *International journal of cancer*, 137(9):2198–2207. 13
- 1615 Kongsgaard, M., Nielsen, C., Hegnsvad, S., Aagaard, P., and Magnusson, S. (2011). Mechanical properties of the human achilles tendon, in vivo. *Clinical Biomechanics*, 26(7):772–777. 43

- Kopans, D. B. (2007). *Breast imaging*. Lippincott Williams & Wilkins. 5, 8, 9, 13
- Krouskop, T. A., Wheeler, T. M., Kallel, F., Garra, B. S., and Hall, T. (1998). Elastic moduli of breast and prostate tissues under compression. *Ultrasonic Imaging*, 20(4):260–274. 40, 41
- ¹⁶²⁰ Kuhlmann, M., Fear, E., Ramirez-Serrano, A., and Federico, S. (2013). Mechanical model of the breast for the prediction of deformation during imaging. *Medical engineering \& physics*, 35(4):470–478. 38, 45
- Lorenzen, J., Sinkus, R., Biesterfeldt, M., and Adam, G. (2003). Menstrual-cycle dependence of breast parenchyma elasticity: estimation with magnetic resonance elastography of breast tissue during the menstrual cycle. *Investigative radiology*, 38(4):236–240. 10, 40
- ¹⁶²⁵ Martin, L. J. (2017). What causes breast cancer? <https://www.webmd.com/breast-cancer/guide/what-causes-breast-cancer>. 11
- ¹⁶³⁰ Martínez-Martínez, F., Rupérez-Moreno, M., Martínez-Sober, M., Solves-Llorens, J., Lorente, D., Serrano-López, A., Martínez-Sanchis, S., Monserrat, C., and Martín-Guerrero, J. (2017). A finite element-based machine learning approach for modeling the mechanical behavior of the breast tissues under compression in real-time. *Computers in Biology and Medicine*, 90:116–124. 38, 40, 43
- ¹⁶³⁵ Mugea, T. T. and Shiffman, M. A. (2014). *Aesthetic Surgery of the Breast*. Springer. 5, 6, 8
- NHSBSP (2012). 2012 review of the uk breast screening programme. <http://www.cancerresearchuk.org/about-cancer/breast-cancer/screening/screening-2012-review>. 12
- ¹⁶⁴⁰ Olgun, D. Ç., Korkmazer, B., Kılıç, F., Dikici, A. S., Velidedeoglu, M., Aydoğan, F., Kantarci, F., and Yilmaz, M. H. (2014). Use of shear wave elastography to differentiate benign and malignant breast lesions. *Diagnostic and Interventional Radiology*, 20(3):239. 14
- Palomar, A. P. d., Calvo, B., Herrero, J., Lpez, J., and Doblar, M. (2008). A finite element model to accurately predict real deformations of the breast. *Medical Engineering & Physics*, 30(9):1089–1097. 38
- ¹⁶⁴⁵ Pandya, S. and Moore, R. G. (2011). Breast development and anatomy. *Clinical obstetrics and gynecology*, 54(1):91–95. 10
- Patete, P., Iacono, M. I., Spadea, M. F., Trecate, G., Vergnaghi, D., Mainardi, L. T., and Baroni, G. (2013). A multi-tissue mass-spring model for computer assisted breast surgery. *Medical Engineering and Physics*, 35(1):47–53. 45

BIBLIOGRAPHY

- Pathmanathan, P., Gavaghan, D. J., Whiteley, J. P., Chapman, S. J., and Brady, J. M. (2008). Predicting tumor location by modeling the deformation of the breast. *IEEE Transactions on Biomedical Engineering*, 55(10):2471–2480. 39, 42, 43, 45
- ¹⁶⁵⁵ Pechter, E. A. (1998). A new method for determining bra size and predicting postaugmentation breast size. *Plastic and reconstructive surgery*, 102(4):1259–1265. 5
- Peters, N. H., Borel Rinkes, I. H., Zuithoff, N. P., Mali, W. P., Moons, K. G., and Peeters, P. H. (2008). Meta-analysis of mr imaging in the diagnosis of breast lesions. *Radiology*, 246(1):116–124. 15
- ¹⁶⁶⁰ Peto, R., Boreham, J., Clarke, M., Davies, C., and Beral, V. (2000). Uk and usa breast cancer deaths down 25% in year 2000 at ages 20–69 years. *The Lancet*, 355(9217):1822. 11
- Pike, M. C., Spicer, D. V., Dahmoush, L., and Press, M. F. (1993). Estrogens progestogens normal breast cell proliferation and breast cancer risk. *Epidemiologic reviews*, 15(1):17–
¹⁶⁶⁵ 35. 11
- Rajagopal, V. et al. (2007). *Modelling breast tissue mechanics under gravity loading*. PhD thesis, ResearchSpace@ Auckland. 45
- ¹⁶⁷⁰ Rajagopal, V., Lee, A., Chung, J.-H., Warren, R., Highnam, R. P., Nash, M. P., and Nielsen, P. M. (2008). Creating individual-specific biomechanical models of the breast for medical image analysis. *Academic Radiology*, 15(11):1425–1436. 38, 40, 41, 42, 43
- Rajagopal, V., Nielsen, P. M. F., and Nash, M. P. (2010). Modeling breast biomechanics for multi-modal image analysis-successes and challenges. *Wiley Interdisciplinary Reviews: Systems Biology and Medicine*, 2(3):293–304. 40
- ¹⁶⁷⁵ Riggio, E., Quattrone, P., and Nava, M. (2000). Anatomical study of the breast superficial fascial system: the inframammary fold unit. *European Journal of Plastic Surgery*, 23(6):310–315. 43
- Ruiter, N. V., Stotzka, R., MULLER, T.-O., Gemmeke, H., Reichenbach, J. R., and Kaiser, W. (2006). Model-based registration of x-ray mammograms and MR images of the female breast. *IEEE Transactions on Nuclear Science*, 53(1):204–211. 38
- ¹⁶⁸⁰ Samani, A. and Plewes, D. (2004). A method to measure the hyperelastic parameters of ex vivo breast tissue samples. *Physics in Medicine and Biology*, 49(18):4395–4405. 41
- Samani, A., Zubovits, J., and Plewes, D. (2007). Elastic moduli of normal and pathological human breast tissues: an inversion-technique-based investigation of 169 samples. *Physics in medicine and biology*, 52(6):1565. 40

BIBLIOGRAPHY

- 1685 Sinkus, R., Tanter, M., Xydeas, T., Catheline, S., Bercoff, J., and Fink, M. (2005). Viscoelastic shear properties of in vivo breast lesions measured by mr elastography. *Magnetic resonance imaging*, 23(2):159–165. 41
- Skandalakis, J. E. (2009). Embryology and anatomy of the breast. *Breast augmentation: principles and practice*. Springer, Berlin, 12. 4
- 1690 SPF (2016). Sante publique france: Cancer du sein. <http://invs.santepubliquefrance.fr/Dossiers-thematiques/Maladies-chroniques-et-traumatismes/Cancers/Donnees-par-localisation/Cancer-du-sein>. 11
- Sturgeon, G. M., Kiarashi, N., Lo, J. Y., Samei, E., and Segars, W. P. (2016). Finite-element modeling of compression and gravity on a population of breast phantoms for multimodality imaging simulation. *Medical Physics*, 43(5):2207–2217. 38, 40, 43
- 1695 Sutradhar, A. and Miller, M. J. (2013). In vivo measurement of breast skin elasticity and breast skin thickness. *Skin Research and Technology*, 19(1). 8, 42
- Tabár, L., Vitak, B., Chen, H.-H. T., Yen, M.-F., Duffy, S. W., and Smith, R. A. (2001). Beyond randomized controlled trials. *Cancer*, 91(9):1724–1731. 12
- 1700 Tanner, C., Schnabel, J. A., Hill, D. L. G., Hawkes, D. J., Leach, M. O., and Hose, D. R. (2006). Factors influencing the accuracy of biomechanical breast models. *Medical Physics*, 33(6):1758. 40
- Ulger, H., Erdogan, N., Kumanlioglu, S., and Unur, E. (2003). Effect of age, breast size, menopausal and hormonal status on mammographic skin thickness. *Skin Research and Technology*, 9(3):284–289. 8
- 1705 Van Houten, E. E., Doyley, M. M., Kennedy, F. E., Weaver, J. B., and Paulsen, K. D. (2003). Initial in vivo experience with steady-state subzone-based mr elastography of the human breast. *Journal of magnetic resonance imaging*, 17(1):72–85. 41
- Vandeput, J. and Nelissen, M. (2002). Considerations on anthropometric measurements of the female breast. *Aesthetic plastic surgery*, 26(5):348–355. 6
- 1710 Vavourakis, V., Hipwell, J. H., and Hawkes, D. J. (2016). An inverse finite element u/p-formulation to predict the unloaded state of in vivo biological soft tissues. *Annals of biomedical engineering*, 44(1):187–201. 39
- Wellman, P., Howe, R. D., Dalton, E., and Kern, K. A. (1999). Breast tissue stiffness in compression is correlated to histological diagnosis. *Harvard BioRobotics Laboratory Technical Report*, pages 1–15. 40, 41
- 1715 Wenger, M. P., Bozec, L., Horton, M. A., and Mesquida, P. (2007). Mechanical properties of collagen fibrils. *Biophysical journal*, 93(4):1255–1263. 43

BIBLIOGRAPHY

- Whelehan, P., Evans, A., Wells, M., and MacGillivray, S. (2013). The effect of mammography pain on repeat participation in breast cancer screening: a systematic review. *The Breast*, 22(4):389–394. 15
1720
- Yaffe, M., Boone, J., Packard, N., Alonzo-Proulx, O., Huang, S.-Y., Peressotti, C., Al-Mayah, A., and Brock, K. (2009). The myth of the 50-50 breast. *Medical physics*, 36(12):5437–5443. 7
- Youk, J. H., Gweon, H. M., and Son, E. J. (2017). Shear-wave elastography in breast ultrasonography: the state of the art. *Ultrasonography*, 36(4):300. 14
1725